

**Strategies to improve the photocatalytic performance of  
covalent triazine frameworks**

Journal:	<i>Journal of Materials Chemistry A</i>
Manuscript ID	TA-REV-07-2023-004472.R1
Article Type:	Review Article
Date Submitted by the Author:	09-Sep-2023
Complete List of Authors:	Liu, Yubing; Nagoya University Wu, Hao; Nagoya University, Department of Materials Science and Engineering Wang, Qian; Nagoya University, Department of Materials Science and Engineering

1     **Strategies to improve the photocatalytic performance of covalent triazine frameworks**

2     Yubing LIU<sup>1,†</sup>, Hao WU<sup>1,†</sup>, Qian WANG<sup>1,2,\*</sup>

3     **Affiliation and full postal address**

4     1 *Graduate School of Engineering, Nagoya University, Furo-cho, Chikusa-ku, Nagoya 464-*  
5     *8603, Japan*

6     2 *Institute for Advanced Research, Nagoya University, Furo-cho, Chikusa-ku, Nagoya 464-*  
7     *8601, Japan*

8     <sup>†</sup>These authors contributed equally to this work.

9     **\*Corresponding author**

10    Professor Qian WANG

11    *Graduate School of Engineering, Nagoya University, Furo-cho, Chikusa-ku, Nagoya 464-*  
12    *8603, Japan*

13    Tel: +81-527893250

14    E-mail: [wang.qian@material.nagoya-u.ac.jp](mailto:wang.qian@material.nagoya-u.ac.jp)

15

16

17 **Abstract**

18 Covalent triazine frameworks (CTFs) have emerged as a prominent group of organic  
19 semiconductors, distinguishing themselves from covalent organic frameworks (COFs) for their  
20 applications in photocatalysis. Their unique features, such as a fully conjugated structure,  
21 triazine unit, interlayer  $\pi$ - $\pi$  interaction, large specific surface area, and exceptional thermal and  
22 chemical stability, make them promising candidates for artificial photosynthetic processes,  
23 including photocatalytic water splitting and CO<sub>2</sub> reduction reactions. However, challenges like  
24 high exciton binding energy and carrier recombination need to be addressed. In this review, we  
25 highlight the latest advances in utilizing CTFs for photocatalytic applications and delve into  
26 strategies aimed at modifying the band structure, enhancing photoexcited carrier separation,  
27 and improving carrier transfer processes in CTFs. These approaches involve molecular design,  
28 structural regulation, and the creation of heterostructures, all aimed at boosting the quantum  
29 efficiency of photocatalytic reactions. These efforts hold tremendous potential for advancing  
30 solar fuel production.

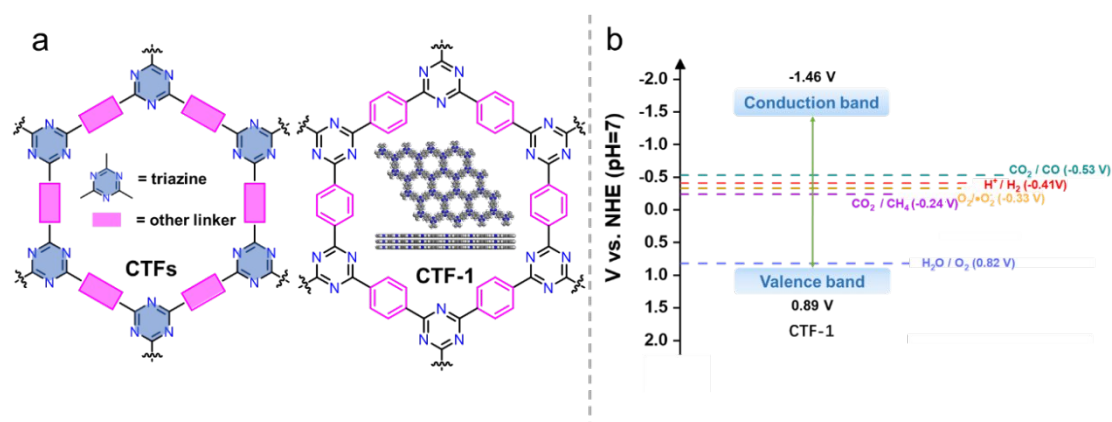
31

32

## 33 1. Introduction

34 As one of the most popular star materials in recent years, covalent organic framework  
35 materials (COFs)<sup>1,2</sup> have been intensively studied in various fields including photocatalysis<sup>3,4</sup>,  
36 electrocatalysis<sup>5</sup>, drug delivery<sup>6</sup>, heterogeneous catalysis<sup>7, 8</sup>, batteries<sup>9</sup> and environmental  
37 applications<sup>10, 11</sup>. Covalent triazine frame materials (CTFs)<sup>12</sup> are a type of covalent organic  
38 framework materials that are generally constructed by connecting different monomers with  
39 triazine rings as linking groups (Figure 1). CTFs, as ordered crystalline organic semiconductor  
40 materials, exhibit the following characteristics: (1) rich N content. The triazine structure as a  
41 connecting group greatly increases the N content of CTFs. This high N content contributes to  
42 the heteroatom effect, resulting in abundant active and functional centers for catalytic  
43 reactions.<sup>13,14</sup> Moreover, the N-rich structure enables CTFs to exhibit certain basic and electron  
44 donor properties.<sup>15, 16</sup> (2) Ordered conjugated structure.<sup>14</sup> The ordered arrangement of triazine  
45 rings and functionalized monomers in the structure of CTFs forms a highly conjugated structure.  
46 This ordered conjugation of crystalline states can facilitate the transport of non-equilibrium  
47 carriers in the excited state and reduce the chance of charge recombination. (3) Large specific  
48 surface area.<sup>17</sup> The ordered in-plane arrangement of monomers in the CTFs structure and the  
49 ordered stacking between layers lead to the formation of regular pore channels. This unique  
50 structure contributes to a large specific surface area, providing a significant number of active  
51 sites for catalytic reactions. (4) Diverse monomer selection.<sup>18</sup> The diverse range of organic  
52 monomers used in the construction of CTFs allows for easy modulation of the optoelectronic  
53 properties of the synthesized CTF materials by altering the monomer composition. This  
54 tunability of properties makes CTFs highly promising for applications in the field of

55 photocatalysis.<sup>19-23</sup> (5) High thermal and chemical stability due to C=N in the triazine  
 56 structure.<sup>24</sup>



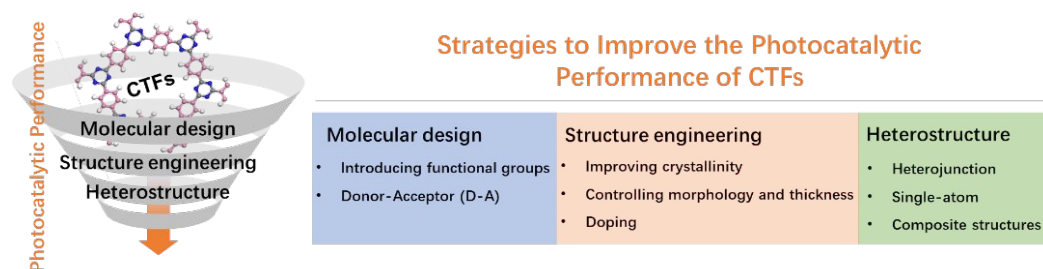
57  
 58 **Figure 1.** (a) The structures of CTF and CTF-1. (b) Energy diagram of CTF-1<sup>25</sup> (<sup>t</sup>BuOK assisted  
 59 synthesis).

60  
 61 Due to the growing scarcity of energy resources and the environmental impact associated  
 62 with the extensive use of fossil fuels, there is an urgent need to explore and develop alternative  
 63 clean energy sources. Converting and storing solar energy into chemical energy via artificial  
 64 photosynthetic processes, such as photocatalysis, offers a promising approach to alleviate the  
 65 reliance on fossil fuels while simultaneously reducing greenhouse gas emissions. These  
 66 processes involve using solar energy to drive water-splitting reaction that produce green  
 67 hydrogen (H<sub>2</sub>) from water and convert CO<sub>2</sub> into high-value carbon-based chemicals and fuels  
 68 (C1 to C4 species).<sup>26-28</sup>

69 Since the groundbreaking work by Fujishima and Honda on water splitting over TiO<sub>2</sub>  
 70 photoelectrodes under UV light irradiation,<sup>29</sup> the field of photocatalyst research has experienced  
 71 rapid development. Efficient photocatalysts are characterized by several key factors, including  
 72 (1) a narrow bandgap to ensure effective utilization of solar energy; (2) suitable conduction and

73 valence band positions to drive desired oxidation and reduction reactions involved in processes  
 74 like proton/ $\text{CO}_2$  reduction and water oxidation; (3) good stability during the photocatalytic  
 75 reaction; (4) low cost; (5) good recyclability; and (6) practicality and feasibility for commercial-  
 76 scale applications.

77 CTFs have demonstrated great potential in terms of controllable energy band structures,  
 78 photocatalytic performance, stability, and cost-effectiveness. However, unmodified CTFs still  
 79 face challenges, including low utilization of visible light, high recombination probability of  
 80 photogenerated carriers, and tight stacking that hinders the exposure of active sites.<sup>13, 30</sup> In this  
 81 review, we investigate the recent advancements in the utilization of CTFs for photocatalytic  
 82 applications, specifically in the areas of water splitting,  $\text{CO}_2$  reduction, and organic  
 83 transformations. We also outline emerging techniques that have been employed to enhance the  
 84 photocatalytic performance of CTFs, including molecular design, structural regulation, and  
 85 heterostructure engineering (Figure 2). Throughout the review, we not only highlight the  
 86 significant findings and achievements in this field but also identify the remaining challenges  
 87 ahead, aiming to provide valuable insights and guidance for the development of new and highly  
 88 efficient photocatalytic systems based on CTFs.



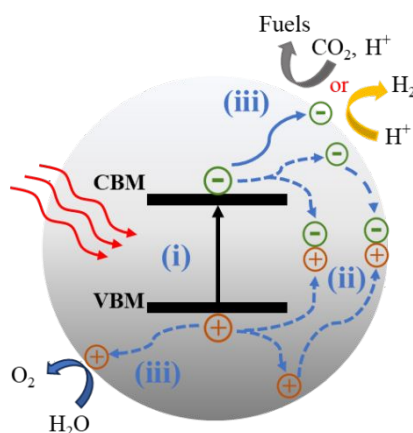
89

90 **Figure 2.** The strategies to improve the photocatalytic performance of CTFs.

91

## 92 2. CFTs for photocatalytic applications

93 Photocatalytic reactions (Figure 3) involve three key steps<sup>27</sup>: (1) Photon absorption:  
94 Photocatalysis begins with photons being absorbed, elevating electrons from the valence band  
95 (VB) to the conduction band (CB) and generating electron-hole pairs ( $e^-/h^+$ ). (2) Charge  
96 separation and migration: Excited electrons and holes move within the photocatalyst material,  
97 concentrating at active surface sites for subsequent reactions. (3) Redox reactions: Accumulated  
98 electron-hole pairs initiate redox reactions facilitated by cocatalysts. Electrons participate in  
99 reduction reactions, while holes engage in oxidation reactions. Thus, the CB minimum must be  
100 more negative than the reduction potential, and the VB maximum must be more positive than  
101 the oxidation potential.



102  
103 **Figure 3.** Scheme of the photocatalytic  $\text{CO}_2$  reduction reaction and water splitting for the  
104 semiconductor. CBM: conduction-band minimum; VBM: valence-band maximum. (i)  
105 Absorption of photons. (ii) Charge separation, migration and recombination. (iii) Surface  
106 reactions.

107

108 To achieve specific photocatalytic reactions, for example, water splitting, an energy  
109 requirement ( $\Delta E$ ) of 1.23 V is necessary to decompose one molecule into  $\text{H}_2$  and  $1/2 \text{O}_2$ ,

110 corresponding to a change in Gibbs free energy of 237.2 kJ/mol. Consequently, the  
111 photocatalyst must possess a bandgap wider than 1.23 V. In practice, a bandgap greater than  
112 1.6 eV is often desired to fulfill additional kinetic requirements.<sup>31</sup> CO<sub>2</sub> is known to be a  
113 thermodynamically stable and chemically inert molecule, making the breaking of the C=O bond  
114 a highly energy-demanding process.<sup>32</sup> Photocatalytic CO<sub>2</sub> reduction is a complex process that  
115 produces various reduction products including gaseous products (CO, CH<sub>4</sub>, etc.) and liquid  
116 products (CH<sub>3</sub>OH, CHOOH, etc.)<sup>33</sup> through single or multiple electron transfer processes.

117 CTFs are well suited for photocatalytic hydrogen production reactions in terms of the  
118 energy band structure. As an example, CTF-1 (Figure 1), the most representative CTFs, has a  
119 bandgap of about 2.35 eV.<sup>25</sup> The valence and conduction band positions (Figure 1b) are suitable  
120 for enabling both hydrogen and oxygen evolution. Additionally, the energy band structure of  
121 CTF-1 can finely be tailored by employing different synthesis methods and selecting different  
122 monomeric raw materials, linkage groups, and functional groups<sup>34</sup>, adjusting the crystallinity  
123 of the material<sup>35</sup>, or introducing donor-acceptor (D-A)<sup>36</sup> structures. These strategies provide  
124 opportunities to optimize the energy band alignment to suit a specific photocatalytic reaction.  
125 Furthermore, the inherent basicity of CTFs<sup>37, 38</sup> and the incorporation of basic functional groups  
126 can enhance the adsorption of CO<sub>2</sub> and promote the activation of CO<sub>2</sub> molecules in  
127 photocatalytic CO<sub>2</sub> reduction reaction<sup>39</sup>, which contribute to enhanced conversion efficiency of  
128 CO<sub>2</sub>, making CTFs promising materials for efficient photocatalytic CO<sub>2</sub> reduction.

129 In the design of photocatalysts, it is desirable for the catalyst to have a wide absorption  
130 range, as approximately 43% of the energy in solar radiation falls within the visible range (400-  
131 700 nm).<sup>27</sup> In the structure of CTFs,  $\pi$ -conjugated units play a crucial role in light absorption,



132 where visible light allows electrons to undergo  $\pi \rightarrow \pi^*$  transition<sup>40</sup>. To enhance the absorption  
133 range of CTFs and improve their photocatalytic performance, specific groups are often  
134 introduced from a structural design perspective.

135 In addition to the stringent thermodynamic requirements, photocatalytic reactions also  
136 face kinetic challenges. The timescales for charge separation, migration of photogenerated  
137 carriers, and surface reactions can range from picoseconds (ps) to milliseconds (ms).<sup>41, 42</sup>  
138 Achieving efficient solar energy conversion requires effective synergy between each step. The  
139 crystal structure, crystallinity, and particle size of the photocatalyst significantly influence  
140 charge separation and migration of photogenerated carriers. CTFs exhibiting poor crystallinity  
141 are often associated with a high density of structural defects. These defects typically function  
142 as sites for the capture and recombination of photogenerated electrons and holes, resulting in a  
143 reduction in quantum efficiency and consequently low photocatalytic activity.<sup>43</sup> Conversely, a  
144 higher crystal quality promotes efficient charge separation and reduces carrier recombination,  
145 enhancing the overall quantum efficiency and photocatalytic performance. Controlling the  
146 particle size is another crucial factor in optimizing photocatalytic activity. Smaller particle sizes  
147 result in a shorter distance between the photogenerated electrons and holes, facilitating their  
148 migration to the surface reaction sites.<sup>44</sup> This reduced distance can also reduce the probability  
149 of carrier recombination, thereby enhancing photocatalytic efficiency. In the case of CTF, their  
150  $\pi$ - $\pi$  layered stacking structure and relatively fewer layers favor the transport of photogenerated  
151 carriers from the bulk phase to the surface through interlayer migration.<sup>13</sup> To further improve  
152 the separation and migration efficiency of photogenerated carriers, related studies have focused  
153 on strategies such as increasing crystallinity, introducing D-A structures, and exfoliating CTFs

154 into oligomeric or monolayer.

155       The last step of surface chemistry involves the presence of active sites on the photocatalyst  
156 surface. Even if photogenerated electrons and holes possess thermodynamically sufficient  
157 redox potentials, they will recombine with each other if there are no active sites available for  
158 redox reactions on the surface. In H<sub>2</sub> evolution reaction (HER), Pt is commonly used as a  
159 cocatalyst. Pt not only promotes charge separation and transport but also acts as a reaction site  
160 to catalyze the HER. However, Pt can also facilitate the oxygen reduction reactions, which is  
161 the reverse reaction of water splitting. This makes Pt unideal for use in overall water splitting  
162 (OWS) processes.<sup>45</sup> To address this, materials such as Ru or Rh have been widely utilized as  
163 alternatives to Pt in promoting the OWS reaction.<sup>46</sup> For the CO<sub>2</sub> reduction reaction (CO<sub>2</sub>RR),  
164 metal-organic complexes are often employed as cocatalysts to provide active centers.<sup>32</sup> The  
165 structural diversity and modifiability of CTFs can offer a rich variety of active sites, while their  
166 high specific surface area and regular pore structure facilitate the construction of numerous  
167 active sites with well-defined structures. This property of CTFs allows for the exploration of  
168 various active site structures and their correlation with photocatalytic performance, serving as  
169 research models for improving photocatalytic performance and elucidating the relationships  
170 between active site structures and overall photocatalytic efficiency.

171

### 172 **3. Strategies for improving the photocatalytic activity of CTFs**

#### 173 **3.1. Molecular design**

##### 174 **3.1.1 Introducing functional groups**

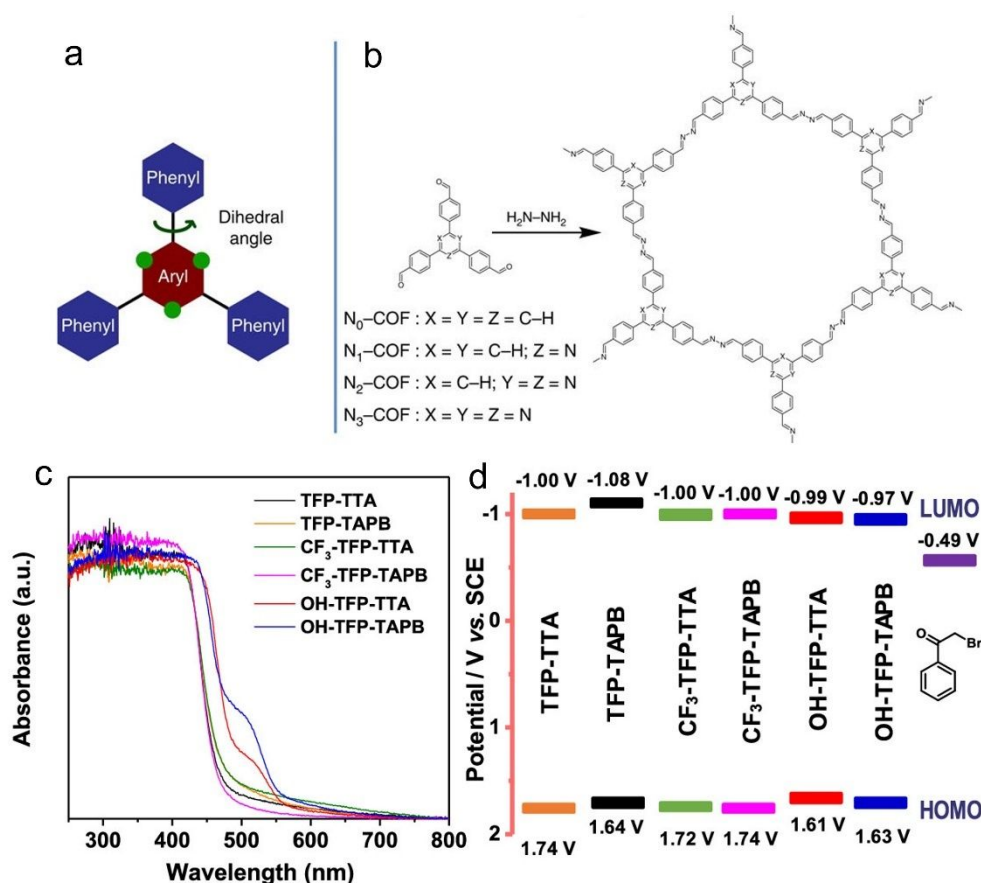
175       CTFs, as organic photocatalytic materials, exhibit strong dependence on their intrinsic

176 photocatalytic performance on their structure. The introduction of novel functional groups is a  
177 promising approach to induce locally inhomogeneous electron distribution in CTFs, leading to  
178 reduced exciton binding energy and enhanced carrier separation. Researchers have been  
179 extensively exploring microstructural modulation strategies to enhance the  
180 photoelectrochemical properties of CTFs by introducing functional moieties around the triazine  
181 ring and designing rational structures (Table 1). Lotsch's group<sup>34</sup> reported a series of azine-  
182 linked COFs ( $N_x$ -COFs) (Figure 4a and b) with varying nitrogen content in the central aryl ring  
183 (0-3 nitrogen atoms). The experimental results showed that the photocatalytic hydrogen  
184 evolution activity of  $N_x$ -COFs increased gradually with the nitrogen content in their central aryl  
185 rings (0 N for phenyl to 3 N for triazine), which was closely correlated with the intrinsic  
186 electronic properties, structure, geometry and morphology of the precursors. Among them,  $N_3$ -  
187 COF, which had a triazine structure, exhibited the highest hydrogen evolution performance in  
188 HER. The same group also investigated the reversal of polarity through nitrogen substitution in  
189 the peripheral aryl ring and emphasized the importance of precise control over the structure,  
190 long-range orderliness, and morphology of COFs through dynamic covalent chemistry.<sup>47</sup>

191 Speybroeck et al.<sup>48</sup> conducted a study combining experimental and theoretical calculations  
192 to investigate the modulation of the large  $\pi$ -system and  $\pi$ -electron defects in CTFs in order to  
193 broaden the absorption range of the spectrum. Their findings revealed that incorporating  
194 aromatic rings, increasing the nitrogen content, or terminating the linker with electron-  
195 withdrawing -CN groups were effective strategies for enhancing the absorption capability. In  
196 the photocatalytic reductive dehalogenation reactions,<sup>49</sup> the introduction of -OH substituents  
197 into the aromatic ring of CTFs resulted in a narrower bandgap compared to -H and -CF<sub>3</sub>

198 substituents, thereby enhancing the photocatalytic activity under green light-emitting diode  
199 (LED) lamp (30 W, 520-530 nm) (Figure 4c and d).

200 Other studies focused on enhancing the transfer of photogenerated electrons by  
201 incorporating phenanthroline<sup>50</sup> and bipyridine units<sup>51, 52</sup> into the CTF backbone through precise  
202 control of the N-site positions at the atomic level. For instance, the incorporation of phenazoline  
203 units in the conjugated Phen-CTF demonstrated improved photoluminescence and strong  
204 photoredox properties. In photocatalytic reactions involving activated carbon-halogen bonds  
205 (C-Br and C-Cl), such as dehalogenation processes, the presence of CTFs facilitated the  
206 formation of C-C, C-P, and C-B bonds through radical trapping under light illumination.  
207 Furthermore, investigations into the photocatalytic HER and OWS of various bipyridine-based  
208 COFs<sup>51-53</sup> revealed that even slight variations in the N sites within COFs can lead to significant  
209 differences in electron transfer and band structures.



210

211 **Figure 4.** (a) The design of a tunable triphenylarene platform for photocatalytic hydrogen

212 evolution under visible light irradiation by using TEOA as sacrificial agents. 'N atoms' replace

213 'C-H' at the green dots and change the angle between the central aryl and peripheral phenyl

214 rings, leading to varied planarity in the platform. (b) Synthesis of  $N_x$ -COFs from  $N_x$ -aldehydes215 and hydrazine. Reproduced with permission from ref.<sup>54</sup>. Copyright 2015, Springer Nature. (c)

216 UV-vis spectra, (d) Schematic energy band structures (vs SCE, reference with the redox

217 potential of 2-bromoacetophenone) of COFs with -OH, -H and - $CF_3$  substituent. Reproduced218 with permission from ref.<sup>49</sup>. Copyright 2020, American Chemical Society.

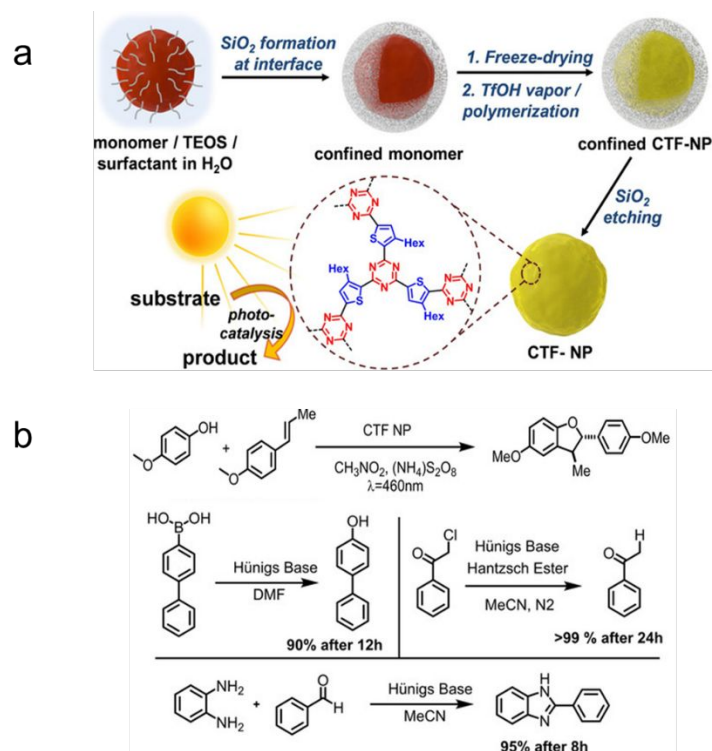
219

220 Jin's group designed and synthesized CTFs based on pyrene (Py)<sup>55</sup> and thiazolo[5,4-221 d]thiazole (TzTz)<sup>56</sup>. The introduction of pyrene, a well-known fluorescent group, into CTF-PY

222 resulted in high activity in photocatalytic HER and CO<sub>2</sub>RR in the presence of triethanolamine  
223 (TEOA) as an electron donor under visible light irradiation ( $\lambda > 420$  nm). On the other hand,  
224 the TzTz moieties in CTF-NWU-1 exhibited excellent light absorption properties and strong  
225 electron acceptor characteristics, leading to a narrower bandgap and enhanced charge  
226 separation ability. In addition to TzTz, other organic sulfides such as thiophene (Th),<sup>57</sup>  
227 thiourea,<sup>58</sup> benzothiadizole (BT)<sup>59, 60</sup> and sulfone<sup>61</sup> are frequently utilized to construct novel  
228 CTF materials containing triazine rings. Thiophene, for instance, possesses a higher dipole  
229 moment, and its incorporation into CTF backbones created a strong internal electric field,<sup>36</sup>  
230 which promoted efficient separation and migration of photogenerated charge carriers, thereby  
231 enhancing the photocatalytic activity in processes such as HER,<sup>36, 57</sup> Ugi reaction, and  
232 functionalization of thiophenols.<sup>62</sup>

233 Liu et al.<sup>63</sup> compared the photocatalytic HER activity of CTF-7 and CTF-8 synthesized  
234 using thiophene and furan as building blocks, respectively. The experimental results revealed  
235 that CTF-7 exhibited better performance than CTF-8 for HER, primarily attributed to its  
236 polarized  $\pi$  electron distribution structure, which facilitated efficient charge separation.  
237 Thiourea derivatives can activate substrates in organocatalytic reactions by forming two  
238 hydrogen bonds through the acidic N-H groups. Building on this concept, the introduction of  
239 thiourea groups in CTFs enhanced their polarization and significantly promoted proton transfer  
240 as well as electron/hole accumulation at the N 2p and C=O/C=S groups.<sup>58</sup> These thiourea  
241 functionalized CTFs were found to activate the two-electron reduction of O<sub>2</sub> to H<sub>2</sub>O<sub>2</sub> without  
242 sacrificial agents or cocatalysts, and the yields of H<sub>2</sub>O<sub>2</sub> increased with the polarity of the  
243 thiourea moieties. Benzothiadizole (BT) moieties are commonly employed in the design of

244 organic photovoltaic materials. By incorporating electron-deficient BT moieties into the  
 245 conjugated structure of CTFs (CTF-BT), the electronic structure can be tuned to enhance the  
 246 performance of various photocatalytic reactions such as  $\text{H}_2\text{O}_2$  production,<sup>59</sup> syntheses of  
 247 dibenzofuran, and formation reactions involving dehalogenation, hydroxylation, and  
 248 benzoimidazole (Figure 5).<sup>60</sup>



249

250 **Figure 5.** (a) Synthetic route of CTF-BT nanoparticles. (b) Four photoredox reactions catalyzed  
 251 by CTF-BT. Reproduced with permission from ref.<sup>60</sup>. Copyright 2020, John Wiley and sons.

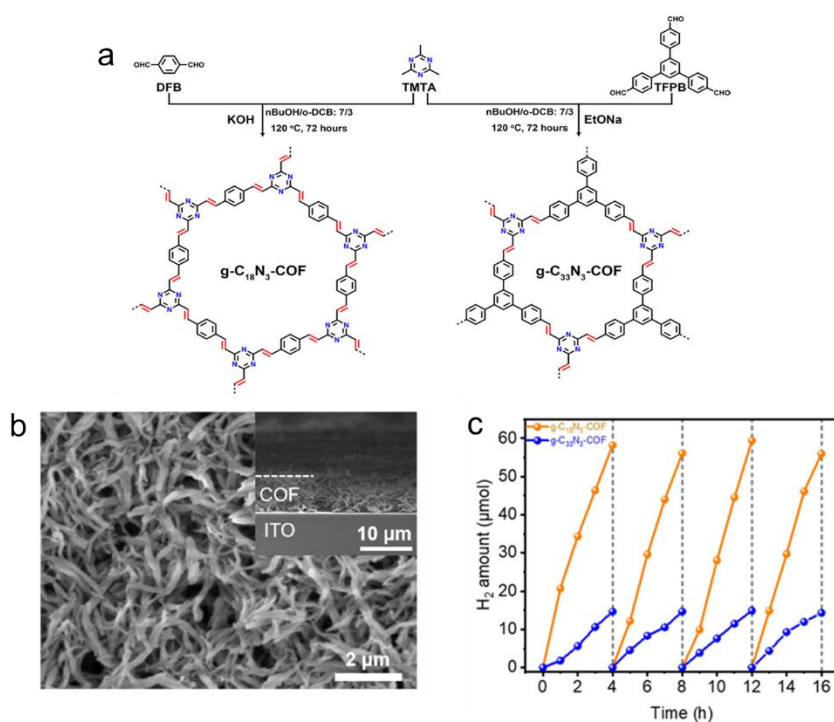
252

253 Cooper et al. synthesized crystalline CTFs using benzobis (benzothiophene sulfone), and  
 254 the obtained CTFs showed much higher HER activity compared to their amorphous or  
 255 semicrystalline counterparts.<sup>61</sup> The experimental data suggest that the high quantum efficiency  
 256 of fused sulfone CTFs was attributed to their crystallinity, strong visible light absorption, and  
 257 wettable hydrophilic pores.

258 The introduction of  $\pi$ -conjugation units effectively expands the  $\pi$ -conjugated system of  
259 CTFs, leading to a broader absorption of visible light and accelerated separation of electrons  
260 and holes. Carbon-carbon double bonds ( $-C=C-$ )<sup>64</sup> and triple bonds ( $-C\equiv C-$ )<sup>65</sup> are considered  
261 as an effective  $\pi$ -bridge unit in organic semiconductor materials, which facilitates the extension  
262 of  $\pi$ -conjugation to improve the charge carrier mobility. Olefin or acetylene-linked COFs  
263 containing these double or triple bonds exhibit exceptional stability compared to their imine or  
264 C-C single-bond linked analogs. Furthermore, these COFs demonstrate intriguing properties  
265 such as magnetic coupling, electrochemical behavior, and photocatalytic activity, allowing their  
266 application in various fields.<sup>53, 66, 67</sup> CTFs that contain  $sp^2$  carbon-conjugated linkages are  
267 renowned for their exceptional chemical stability and extended electron delocalization. These  
268 unique features have made them highly sought-after for various photocatalytic applications. For  
269 instance, researchers have utilized a Knoevenagel condensation approach to synthesize  $sp^2$ -  
270 carbon-linked COFs with well-defined, crystalline honeycomb-like structures (Figure 6).<sup>68</sup> The  
271 obtained triazine-cored COFs with microfibrillar morphologies were used for the fabrication of  
272 thin film photoelectrodes, which exhibited good photocatalytic HER activity in the presence of  
273 ascorbic acid (AA) as electron donor under visible light irradiation. Additionally, a novel  $sp^2$ -  
274 carbon triazine-based COF has been synthesized using acid-catalyzed Aldol reaction, which  
275 exhibited satisfactory efficiency and reusability in organic dyes photodegradation as well as C-  
276 H functionalization of heteroarenes and arenes.<sup>69</sup> Electron spin resonance (ESR) spectroscopy  
277 has revealed the generation of superoxide radical anions as the dominant species responsible  
278 for degrading organic dyes, thus expanding the applications of  $sp^2$ -carbon triazine-based COFs  
279 to photocatalytic aerobic reactions. For instance, olefin-linked CTFs have demonstrated



280 selective oxidation of phenyl methyl sulfide with O<sub>2</sub> under blue light irradiation.<sup>70, 71</sup>



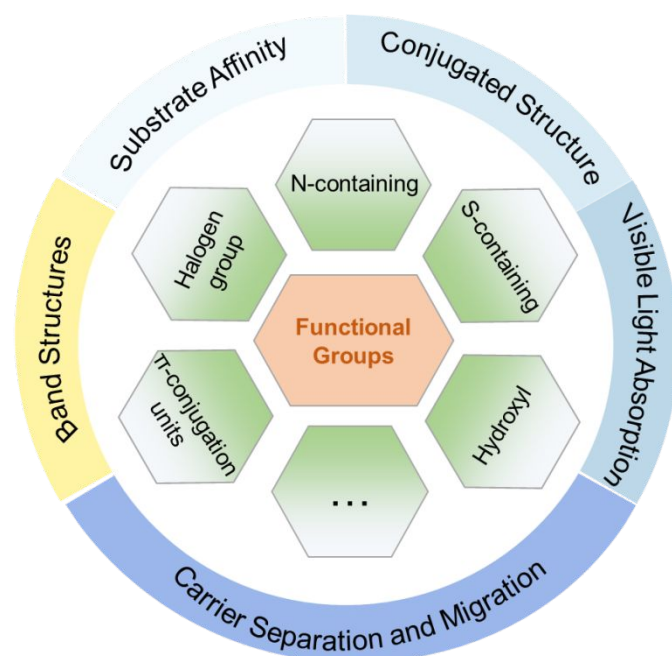
281

282 **Figure 6.** (a) Rational synthesis of g-C<sub>18</sub>N<sub>3</sub>-COF and g-C<sub>33</sub>N<sub>3</sub>-COF by Knoevenagel  
 283 condensation. (b) The scanning electron microscopy (SEM) micrograph of g-C<sub>18</sub>N<sub>3</sub>-COF film  
 284 from top view. (c) Photocatalytic H<sub>2</sub> evolution of g-C<sub>18</sub>N<sub>3</sub>-COF and g-C<sub>33</sub>N<sub>3</sub>-COF under visible  
 285 light irradiation by using ascorbic acid as sacrificial agents. Reproduced with permission from  
 286 ref.<sup>68</sup>. Copyright 2020, American Chemical Society.

287

288 The incorporation of acetylene (-C≡C-) or diacetylene (-C≡C-C≡C-) moieties in CTFs has  
 289 been found to inhibit backward charge recombination, thereby extending the lifetime of charge  
 290 carrier migration from the donor to the acceptor. These -C≡C- and -C≡C-C≡C- moieties can  
 291 significantly reduce the formation energy of OH\* and facilitate a two-electron oxidation  
 292 pathway for producing H<sub>2</sub>O<sub>2</sub>.<sup>72</sup> The spatial separation between the triazine and acetylene cores  
 293 further enhances charge separation and migration.<sup>73</sup> Acetylene-bridged CTFs have

294 demonstrated good performance in the selective oxidation of sulfides and oxidative coupling  
295 of amines under visible light irradiation.<sup>74, 75</sup> Optical and electronic analyses have demonstrated  
296 that the introduction of vinylene and acetylene moieties into the CTF skeleton promoted  
297 accelerated charge mobility and improved the visible light absorption capacity.<sup>74</sup> The acetylene  
298 moiety, serving as a  $\pi$ -cross-linker within the framework, plays a crucial role in promoting  
299 exciton dissociation, minimizing exciton binding energy, and enhancing oxygen adsorption  
300 capacity for facilitating  $O_2^{\bullet -}$  and  $^1O_2$  formation in oxidative coupling reactions.<sup>75</sup> CTFs  
301 containing triazine rings linked by both vinyl and acetylene groups, such as COF-TMT-A, have  
302 exhibited excellent performance in photocatalytic  $CO_2RR$ .<sup>76</sup> In comparison to CTFs without  
303 acetylene groups, these materials demonstrated significantly improved photocatalytic  
304 performance for  $CO_2RR$ , with a remarkable 99% selectivity towards the product  $HCOO^-$ .



305

306 **Figure 7.** The roles of specific functional groups in modulating the characteristics of CTFs.

307

308 Obviously, the introduction of specific functional groups plays a pivotal role in modulating  
 309 the substrate affinity, conjugated structure, and inherent photoelectric characteristics of CTFs  
 310 (Figure 7). This modulation is advantageous for enhancing the adsorption of reaction substrates  
 311 and facilitating the separation and transport of photogenerated electrons and holes. The  
 312 deliberate design of CTFs with innovative and well-thought-out structures shows immense  
 313 potential to boost the efficiency of photocatalytic reactions. It is important to note, however,  
 314 that CTFs currently tend to display suboptimal photocatalytic performance when hosting  
 315 various functional groups on their surface simultaneously.

316

317 **Table 1.** Photocatalytic performance of CTFs with different functional groups.

Functional groups	Photocatalyst	Reaction	Reactants	Light source	Production	Ref
N <sub>x</sub>	5 mg N <sub>3</sub> -COF	HER	H <sub>2</sub> O+TEOA <sup>a</sup>	300 W Xe	1703 μmol·h <sup>-1</sup> ·g <sup>-1</sup>	54
	0.68 wt% Pt			lamp (900 > λ > 420 nm)	AQY <sup>c</sup> =0.44%	
Pyrene	50 mg CTF-Py	HER	H <sub>2</sub> O+TEOA	300 W Xe	3080 μmol·h <sup>-1</sup> ·g <sup>-1</sup>	55
	3 wt% Pt			lamp (λ > 420 nm)		
Thiazolo[5,4- d]thiazole	10 mg CTF-NWU-1	HER	H <sub>2</sub> O+TEOA	300 W Xe	17600 μmol·h <sup>-1</sup> ·g <sup>-1</sup>	56
	3 wt% Pt			lamp (λ > 420 nm)	AQY=0.2% at 420 nm	
Thiophene	30 mg ThPy-CPP	HER	H <sub>2</sub> O+TEOA	300 W Xe	16690 μmol·h <sup>-1</sup> ·g <sup>-1</sup>	36
	10 mL 1-Methyl-2-			lamp (λ > 420 nm)	AQY=4.59 % at 420	

	pyrrolidinone			420 nm)	nm	
Thiophene	20 mg CMP-1	HER	H <sub>2</sub> O+TEOA	300 W Xe	9698.53 $\mu\text{mol}\cdot\text{h}^{-1}\cdot\text{g}^{-1}$	<sup>57</sup>
	3 wt% Pt			lamp ( $\lambda >$	AQY=1.57% at 420	
				420 nm)	nm	
Sulfone	5 mg FS-COF	HER	H <sub>2</sub> O+AA <sup>b</sup>	300 W Xe	16300 $\mu\text{mol}\cdot\text{h}^{-1}\cdot\text{g}^{-1}$	<sup>61</sup>
	$\approx$ 4 wt% Pt			lamp ( $\lambda >$	EQE <sup>d</sup> = 3.2% at 420	
				420 nm)	nm	
Thiophene and furan	10 mg CTF-7	HER	H <sub>2</sub> O+ TEOA	visible light	7430 $\mu\text{mol}\cdot\text{h}^{-1}\cdot\text{g}^{-1}$	<sup>63</sup>
	1 wt% Pd			irradiation		
				( $\lambda >$ 420 nm)		
-C=C-	50 mg g-C <sub>18</sub> N <sub>3</sub> -COF	HER	H <sub>2</sub> O+AA	visible light	292 $\mu\text{mol}\cdot\text{h}^{-1}\cdot\text{g}^{-1}$	<sup>68</sup>
	3 wt% Pt			irradiation	AQY=1.06% at 420	
					nm	
Pyrene	10 mg CTF-Py	CO <sub>2</sub> RR	H <sub>2</sub> O+TEOA	300 W Xe	CO selectivity: 95.4%	<sup>55</sup>
	5 $\mu\text{mol}$ Co (II)			lamp ( $\lambda >$	1373 $\mu\text{mol}\cdot\text{h}^{-1}\cdot\text{g}^{-1}$	
	bipyridine			420 nm)		
	complexes					

318 <sup>a</sup>TEOA: triethanolamine, <sup>b</sup>AA: ascorbic acid, <sup>c</sup>AQY: apparent quantum yield, <sup>d</sup>EQE: external quantum efficiency

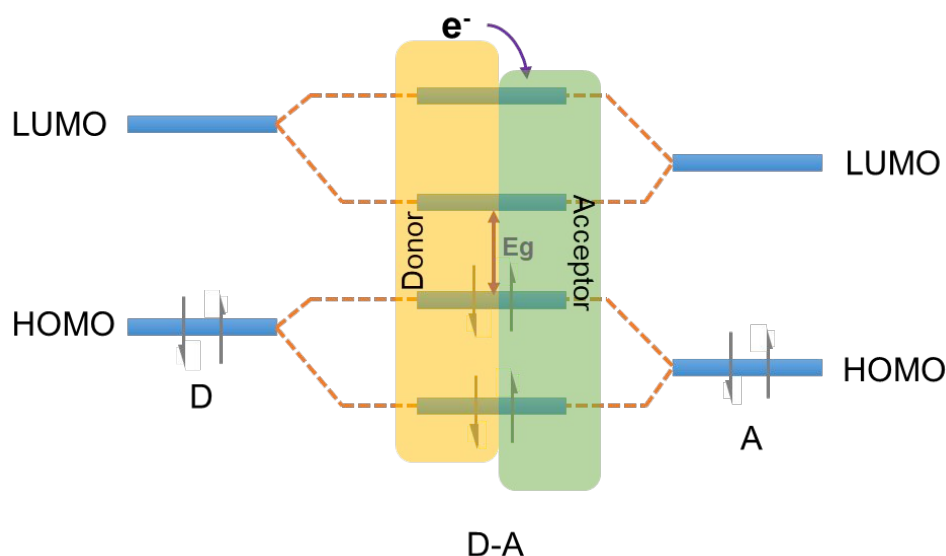
319

### 320 3.1.2 Donor-Acceptor (D-A)

321 The effective inhibition of charge recombination by employing multiple electron donors

322 and acceptors in natural photosynthetic system II promotes the separation of photogenerated

323 electrons, which is attributed to the presence of a photo-induced electron transfer system  
324 composed of multiple donors and acceptors with energy gradients.<sup>77</sup> Furthermore, the covalent  
325 linkage of electron donors (D) with high HOMO energy levels and electron acceptors (A) with  
326 low LUMO energy levels allows for the formation of conjugated D-A molecules and  
327 macromolecules (Figure 8). These structures exhibit tunable LUMO and HOMO energies, as  
328 well as absorption spectra and optical bandgap, resulting from the intramolecular D-A  
329 interactions. Inspired by these principles, the design of organic donors-acceptors structures has  
330 gained significant attention and has been widely explored in various fields, including  
331 photocatalysis<sup>78-80</sup>, organic photovoltaics (OPVs)<sup>81</sup>, organic light-emitting diode (OLED)  
332 materials<sup>82</sup>, and molecular sensors.<sup>83</sup>



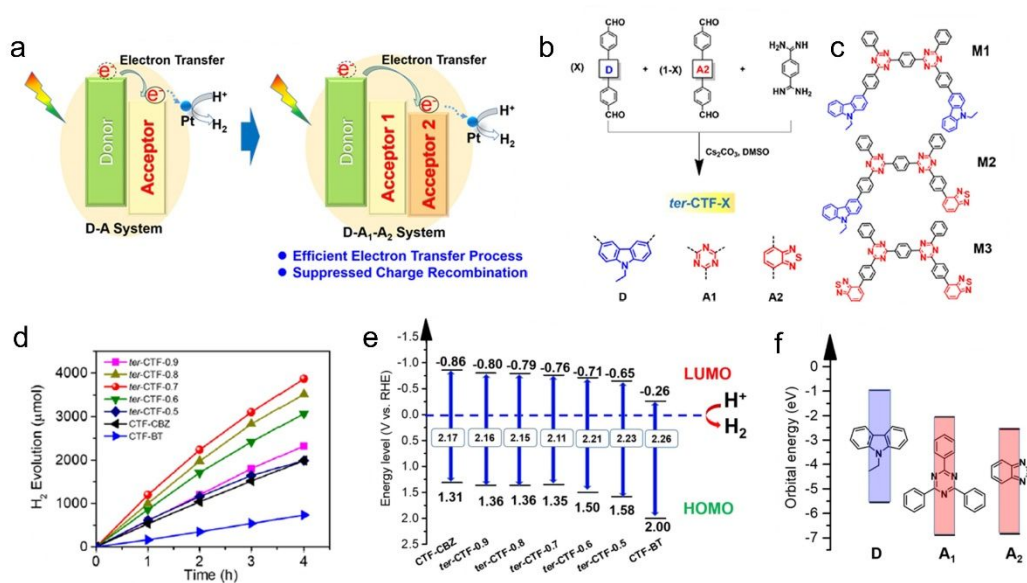
333  
334 **Figure 8.** The effect of orbital coupling of donor and acceptor units on the bandgap and the  
335 transfer path of photogenerated electrons.

336  
337 The strategic modification of CTFs with donor-acceptor (D-A) units can enable the fine-  
338 tuning of their properties and facilitate anisotropic charge carrier migration, thereby enhancing

339 the photocatalytic activity of CTFs. Recent studies have explored various D-A units, such as  
340 thiophene (Th)<sup>36, 84, 85</sup>, thieno[2,3-b]thiophene<sup>86</sup>, phenyl<sup>87</sup>, amide<sup>88</sup>, benzodifuran (BDF)<sup>89</sup>,  
341 naphthalene<sup>90</sup>, carbazole<sup>80, 91</sup>, triphenylamine<sup>92</sup>, benzodithiophene (BDT)<sup>93</sup>, phenothiazine  
342 (PTZ)<sup>94</sup> as electron donors and benzothiadiazole (BT)<sup>80, 84</sup> as electron acceptors to design CTF  
343 for photocatalytic applications (Table 2). Notably, in these D-A CTF materials, the role of  
344 triazine can vary, acting as either an electron donor or acceptor within the CTF structure, owing  
345 to the various electronic properties between triazine and the aforementioned moieties.<sup>85, 87, 91-93</sup>

346 Thiophene or benzothiadiazole (BT) units have been introduced as dopants to enhance the  
347 charge carrier separation and migration in CTF-based photocatalysts. Experimental results and  
348 density functional theory (DFT) calculations have demonstrated that CTFs modified with Th  
349 or BT exhibit extended absorption of visible light and more efficient charge carrier transfer  
350 compared to pristine CTF-1.<sup>84</sup> The incorporation of Th in the CTF framework promoted  $\pi$ -  
351 electron delocalization and facilitated charge transfer, as supported by DFT calculations.<sup>85</sup> As  
352 a result, CTF-Th demonstrated remarkable photocatalytic activity in the hydrogenation of  
353 maleic acid and furfural, leading to the production of succinic acid and furfuryl alcohol,  
354 respectively. In addition, the introduction of a D (carbazole)-A1 (triazine)-A2  
355 (benzothiadiazole) system led to a dramatically improved apparent quantum yield (AQY) of  
356 CTF to 22.8% at 420 nm, surpassing the performance of most conjugated porous polymers,  
357 which typically achieve AQYs within the range of 10% (Figure 9).<sup>80</sup> The bandgap of CTF-1  
358 can be tuned in the range of 2.11 to 2.26 eV by adjusting the ratio of A2 in the structure and the  
359 LUMO energy values of CTF-1 became less negative as the amount of BT increased (Figure  
360 9e). To create molecular heterostructures, CTF-BT/Th was synthesized by incorporating

361 benzothiadiazole (an electron-withdrawing unit) and thiophene (an electron-donating unit) into  
 362 the covalent triazine frameworks through sequential polymerization.<sup>95</sup> The resulting CTF-  
 363 BT/Th exhibited a staggered bandgap arrangement at the heterojunction, resulting in  
 364 significantly improved efficiency in charge carrier separation.



365  
 366 **Figure 9.** (a) The photoinduced electron-transfer process of the D-A system and D-A1-A2  
 367 system. (b) Rational synthesis of ter-CTF-X (X refers to the percentage of M-CBZ in the total  
 368 aldehyde monomers). (c) Three proposed model fragments in ter-CTF-X (M1: CBZ combined  
 369 with triazine; M2: CBZ combined with triazine and BT; and M3: BT combined with triazine).  
 370 (d) Temporal photocatalytic H<sub>2</sub> evolution over CTFs under visible light by using TEOA as  
 371 sacrificial agents. (e) The proposed energy alignments of CTFs based on experimental results.  
 372 (f) The theoretical energy levels of building blocks. Reproduced with permission from ref.<sup>80</sup>.

373 Copyright 2019, American Chemical Society.

374

375 A series of BDT-based CTFs were synthesized to investigate the structure-activity  
 376 relationship in these materials with different D-A ratios.<sup>93</sup> The experimental results showed that

377 an appropriate D-A ratio in BDT-based CTFs led to efficient charge separation and low  
378 electron-hole recombination rates, which greatly promoted the photocatalytic activity for HER.

379 The phenothiazine (PTZ) unit, known for its electron-rich tricyclic heteroaromatic  
380 structure containing strong electron-donating N and S atoms, is commonly utilized as an  
381 electron donor or hole transport material. Incorporating the PTZ unit in CTF resulted in a broad  
382 visible light absorption range of CTF-PTZ. Additionally, CTF-PTZ demonstrated efficient  
383 charge separation and transfer, yielding a significant enhancement in the photocatalytic  
384 performance for the selective aerobic oxidation of sulfides to sulfoxides.<sup>94</sup>

385 Zhang et al. synthesized D-A CTFs containing thiophene (Th)<sup>96</sup>, diphenyl-thiophene (Th-  
386 Ph<sub>2</sub>) and diphenyl-benzothiadiazole (BT-Ph<sub>2</sub>)<sup>97</sup> units directly on the surface of mesoporous  
387 silica (SBA-15). This approach aimed to combine the advantageous properties of both SBA-15  
388 and D-A CTFs to form SBA-15-supported D-A CTFs catalysts. These catalysts exhibited a high  
389 specific surface area, water compatibility, and demonstrated excellent photocatalytic  
390 performance in various reactions, such as the degradation of organic dyes, selective oxidation  
391 of styrene, selective oxidation of alcohols<sup>98</sup> and partial oxidation of 5-hydroxymethylfurfural<sup>99</sup>.  
392 Notably, these reactions were carried out in a solvent-free and solid-state environment,  
393 showcasing the potential of SBA-15-supported D-A CTFs catalysts as efficient and versatile  
394 photocatalytic materials.

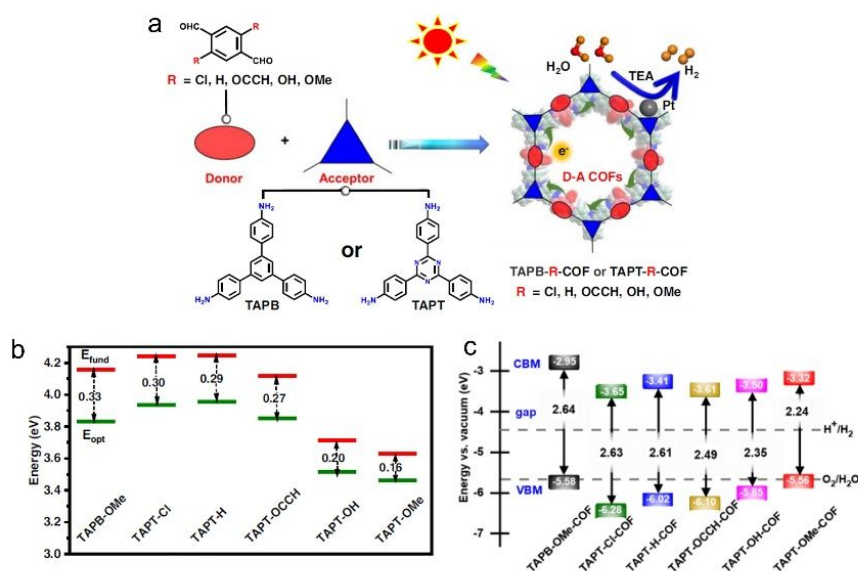
395 The introduction of different functional groups on the donor or acceptor units in D-A CTFs  
396 has a significant impact on their photoelectric properties. For instance, two CTFs containing  
397 naphthalene moieties (with and without methoxy groups) exhibited variations in morphology,  
398 CO<sub>2</sub> adsorption capacity, and optical properties. The presence of methoxy groups on the



399 naphthalene core also influenced these properties.<sup>90</sup> Additionally, both DFT calculations and  
400 experimental results indicated that the conversion of the cyano group to amide functional  
401 groups led to a decrease in the bandgap of the CTF from 2.64 eV to 2.29 eV.<sup>88</sup> The incorporation  
402 of amide groups as electron donors enhanced the visible light absorption and modified the band  
403 structure of the CTFs, thereby promoting the migration and separation of photogenerated  
404 charges. Jiang's group conducted DFT calculations to investigate the band alignment and charge  
405 transfer properties of potential D-A COFs employing various functional groups of tereph-  
406 thaldehydes as donors (Figure 10).<sup>100</sup> The exciton binding energy ( $E_b$ ) is directly associated  
407 with the exciton effect exhibited by these COFs and the relative value of  $E_b$  corresponds to the  
408 strength of the D-A interactions. The activity trends of the COFs, as determined from the  
409 calculated and experimental data, aligned with the exciton effects predicted by DFT. This  
410 computer-aided design approach, enabling precise molecular structure tuning, contributes to  
411 the advancement of photocatalysts with exceptional performance.

412 The one-atom substitution approach is commonly employed to design D-A-type  
413 conjugated porous polymers with specific optical bandgap and aromatic properties.<sup>101</sup> For  
414 instance, when using the same electron donor (pyrazole), CTFs with benzothiadiazole (S atom)  
415 as the electron acceptor exhibited superior photocatalytic HER activity from water compared  
416 to those with 2,1,3-benzoselenadiazole (Se atom) and 2,1,3-benzoxadiazole (O atom). The  
417 stronger electron acceptor, 2,1,3-benzoxadiazole (O atom), resulted in a broader bandgap and  
418 a more negative LUMO energy level, leading to poorer photocatalytic activity. Conversely, the  
419 weaker electron acceptor, 2,1,3-benzoselenadiazole (Se atom), caused a red shift in the  
420 absorption edge of visible light. However, it also led to an increase in bond length and a

421 decrease in acceptor aromaticity, which negatively impacted the intramolecular charge transfer  
 422 process and increased the electron-hole recombination rate. Furthermore, the substitution of  
 423 fluorine atoms on the edge aromatic units improved the crystallinity and porosity of CTFs,  
 424 which was beneficial for the efficient charge transfer of photogenerated carriers.<sup>102</sup> The  
 425 resulting F- substituted CTFs exhibited enhanced O<sub>2</sub> chemisorption and achieved remarkable  
 426 H<sub>2</sub>O<sub>2</sub> yield rates under visible light illumination ( $\lambda > 400$  nm). CTFs with S heteroatoms  
 427 exhibited 5.6 times higher H<sub>2</sub> evolution activity from H<sub>2</sub>O compared to CTFs with O  
 428 heteroatoms.<sup>63</sup> Gaussian and Mulliken calculations revealed that the migration of excited  
 429 electrons from S heteroatoms to triazine units was more efficient than from O heteroatoms in  
 430 CTFs. Electron paramagnetic resonance (EPR) spectra also indicated the generation of a greater  
 431 number of electrons and holes in CTFs with S heteroatoms.



432  
 433 **Figure 10.** (a) D-A COFs constructed by amine monomers and functionalized tereph-  
 434 thalaldehydes for photocatalytic H<sub>2</sub> evolution under 300 W Xe lamp ( $\lambda > 380$  nm) by using  
 435 triethylamine as sacrificial agents. The TAPB, TAPT and TEA indicate 1,3,5-tris(4-  
 436 aminophenyl)benzene, 1,3,5-tris(4-aminophenyl)triazine and triethylamine, respectively. (b)

437 Extrapolation results of fundamental gap ( $E_{\text{fund}}$ , red line) and optical gap ( $E_{\text{opt}}$ , green line)  
438 energies of D-A pairs.  $E_{\text{b}}$  (exciton binding energy) =  $E_{\text{fund}} - E_{\text{opt}}$ . (c) The calculated bandgap and  
439 band position of COFs relative to the vacuum level. The dashed lines are the redox potential of  
440 water at pH = 0. Reproduced with permission from ref.<sup>100</sup>. Copyright 2023, Springer Nature.

441 Protonation of CTFs has been demonstrated to enhance their hydrophilicity and increase  
442 the concentration of water molecules around the catalytic site.<sup>103</sup> This protonation process leads  
443 to an obvious red-shift in light absorption, a substantial increase in charge separation efficiency,  
444 and an overall improvement in the hydrophilic properties of D-A-type imine-linked COFs, and  
445 thus enhanced photocatalytic performance.<sup>104</sup>

446 The extensive repertoire of organic molecules offers a diverse range of options for  
447 constructing CTFs, thereby bestowing them with remarkable structural versatility. Through  
448 meticulous and rational design strategies at the molecular level, precise control over the  
449 selection of precursor molecules exhibiting suitable electronic and spatial characteristics  
450 becomes achievable. This deliberate molecular engineering enables the fine-tuning of the  
451 structural and optoelectronic properties of CTFs, thereby enhancing their photocatalytic  
452 performance. The ability to modulate molecular structures plays a pivotal role in dictating the  
453 intricate relationship between structure, property, and activity in these materials.

454 The strategy of constructing D-A structures has been proved to be effective in designing  
455 novel CTFs. By adjusting the degree of conjugation and electron affinity between the donor  
456 and acceptor, the absorption spectral range of CTFs is broadened, the exciton binding energy  
457 is reduced, and the photogenerated carriers are effectively separated and migrated in D-A CTFs.  
458 Currently, D-A CTFs are mainly constructed using binary monomers via covalent bonds, and

459 there are still limited CTFs with ternary or poly D-A structures (e.g., D-A1-A2, D1-D2-A1,  
 460 D1-A1-D2, etc.). Moreover, the choice of donor and acceptor and how to design a reasonable  
 461 structure to maximize the advantages of the D-A structure are still in the theoretical stage.  
 462 Further research is needed to explore these possibilities.

463 **Table 2.** Photocatalytic performance of CTFs modified with different D-A structures.

Donor	Acceptor	Photocatalyst	Reaction	Reactants	Light source	Production	Ref
Carbazole	Triazine	50 mg ter-CTF-0.7	HER	H <sub>2</sub> O+T	300 W Xe lamp	19300	80
	Benzothiadiazole	2 wt% Pt		EOA <sup>a</sup>	(λ > 420 nm)	μmol·h <sup>-1</sup> ·g <sup>-1</sup> AQY <sup>c</sup> =22.8% at 420 nm	
Thiophene	Benzothiadiazole	50 mg CTF-0.5BT	HER	H <sub>2</sub> O+T	300 W Xe lamp	2240 μmol·h <sup>-1</sup>	84
				EOA	(λ > 420 nm)	l·g <sup>-1</sup> AQY=4% at 420 nm	
Thiophene	Benzothiadiazole	50 mg CTF-BT/Th-1	HER	H <sub>2</sub> O+T	300 W Xe lamp	6600 μmol·h <sup>-1</sup>	95
		3 wt% Pt		EOA	(λ > 420 nm)	l·g <sup>-1</sup> AQE=7.3% at 420 nm	
Benzodifuran	Tris-(4-	10 mg BDF-TAPT-	HER	H <sub>2</sub> O+A	300 W Xe lamp	1390 μmol·h <sup>-1</sup>	89
	aminophenyl)	COF		A	(λ > 420 nm)	l·g <sup>-1</sup>	
	triazine	8 wt% Pt				AQY=7.8% at	

						420 nm	
Fluorene	Triazine	50 mg CTF-N	HER	H <sub>2</sub> O+T	300 W Xe lamp	10760	<sup>91</sup>
		2.11 wt% Pt		EOA	( $\lambda > 420$ nm)	$\mu\text{mol}\cdot\text{h}^{-1}\cdot\text{g}^{-1}$	
						AQY=4.07%	
						at 420 nm	
Pyrazole	Benzothiadiazole	50 mg P1	HER	H <sub>2</sub> O+T	300 W Xe lamp	1000 $\mu\text{mol}\cdot\text{h}^{-1}$	<sup>101</sup>
		3 wt% Pt		EOA	( $\lambda > 420$ nm)	$\text{l}\cdot\text{g}^{-1}$	
						AQE=1.43%	
						at 420 nm	
Triphenylamine	Triazine	3 mg TtaTfa	HER	H <sub>2</sub> O+A	300 W Xe lamp	20700	<sup>104</sup>
		8 wt% Pt		A <sup>b</sup>	( $\lambda > 420$ nm)	$\mu\text{mol}\cdot\text{h}^{-1}\cdot\text{g}^{-1}$	
						AQE=1.43%	
						at 450 nm	
Triazine	Benzodithiophene	20 mg BDTCTF-1	HER	H <sub>2</sub> O+T	300 W Xe lamp	4500 $\mu\text{mol}\cdot\text{h}^{-1}$	<sup>105</sup>
		3 wt% Pt		EOA	( $\lambda > 420$ nm)	$\text{l}\cdot\text{g}^{-1}$	
						AQY=3.9% at	
						420 nm	
Triphenylamine	Triazine	30 mg DA-CTF	CO <sub>2</sub> RR	H <sub>2</sub> O+	300 W Xe lamp	4 $\mu\text{mol CO}$	<sup>92</sup>
		3 $\mu\text{mol CoCl}_2\cdot 6\text{H}_2\text{O}$		MeCN	( $\lambda > 420$ nm)	after one hour	
		0.1 mmol 2,2'-		+TEO		3 $\mu\text{mol H}_2$	
		bipyridine		A		after one hour	

464 <sup>a</sup>TEOA: triethanolamine, <sup>b</sup>AA: ascorbic acid, <sup>c</sup>AQY: apparent quantum yield

## 465 **3.2 Structure engineering**

### 466 **3.2.1 Improving crystallinity**

467 Generally, high crystallinity in materials is associated with reduced defect density and  
468 trapping centers for photogenerated electron-hole trapping and recombination, which in turn  
469 promote efficient charge separation and minimize recombination.<sup>106, 107</sup> Improving the  
470 crystallinity of CTFs is an effective approach to enhance their photocatalytic performance.<sup>35</sup>  
471 Crystalline CTFs offer several advantages over amorphous counterparts, including few  
472 defects<sup>18</sup>, tunable bandgap<sup>25, 108</sup>, uniform porosity<sup>109</sup> and regular crystal plane<sup>110</sup>. Consequently,  
473 researchers have focused on enhancing the crystallinity of CTFs to harness their improved  
474 optical and electronic properties for enhanced photocatalytic activity.

475 Unlike the synthesis of typical COFs, achieving high crystallinity in CTFs poses a  
476 challenge due to the inherent stability of the triazine ring. The dynamic processes of covalent  
477 bond breaking and self-healing are not easily applicable to CTFs. Nevertheless, several methods  
478 have been developed to synthesize CTFs, such as ionothermal method,<sup>111-115</sup> superacid-  
479 catalyzed method,<sup>109, 116-119</sup> polycondensation method<sup>25, 120-122</sup>, P<sub>2</sub>O<sub>5</sub><sup>123</sup> catalyzed method. For a  
480 more comprehensive exploration of COF synthesis methods, we direct the reader to refer to  
481 previous in-depth reviews on this topic.<sup>14,35</sup>

482 CTFs have been synthesized using the high-temperature ZnCl<sub>2</sub> ionothermal route.  
483 However, the resulting CTFs had low crystallinity due to the irreversible carbonization process  
484 and reversible trimerization of nitrile, which allowed for the reorganization of the dynamic  
485 triazine backbone during synthesis.<sup>124, 125</sup> To mitigate the carbonization of the CTF skeleton, a  
486 three-salt eutectic mixture (NaCl/KCl/ZnCl<sub>2</sub>) was introduced as an alternative to pure ZnCl<sub>2</sub>.

487 This approach enabled the synthesis of CTFs at lower temperatures while maintaining the  
488 desired crystallinity.<sup>126, 127</sup>

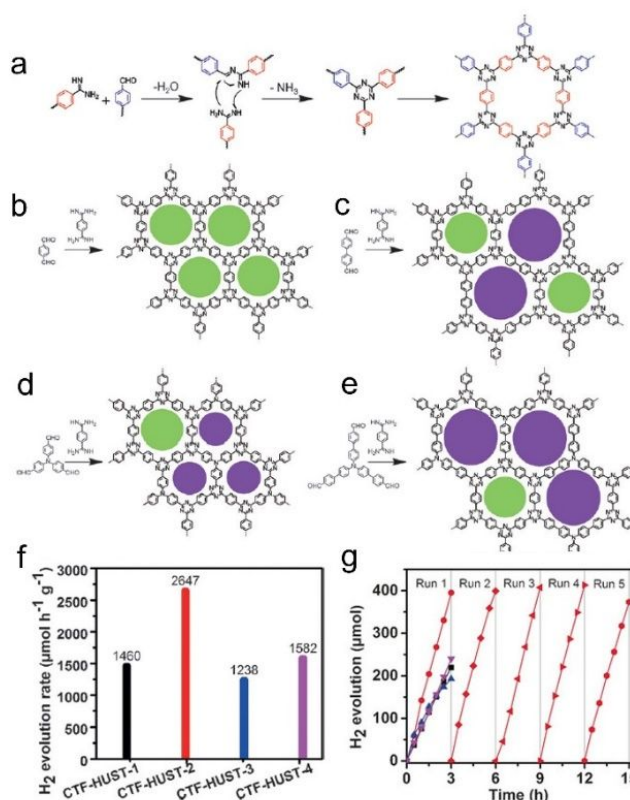
489 Strong Brønsted acids, especially trifluoromethanesulfonic acid ( $\text{CF}_3\text{SO}_3\text{H}$ )<sup>109, 116, 128</sup>, are  
490 widely used catalysts for nitrite trimerization reactions in CTF synthesis, enabling lower  
491 temperature preparation. However, direct synthesis of CTFs using  $\text{CF}_3\text{SO}_3\text{H}$  often results in  
492 low crystallinity. To address this issue, microwave-assisted methods have been developed to  
493 enhance crystallinity by promoting dynamic triazine association and dissociation at lower  
494 temperatures.<sup>104</sup> Microwave-assisted polymerization of highly ordered CTF-1 exhibited  
495 increased crystallinity with higher microwave power, although excessive power can distort the  
496 structure by damaging hexagonal units and extending layer distance.<sup>129</sup> Xu's group successfully  
497 developed a rapid and scalable microwave-assisted synthesis method for preparing a series of  
498 highly crystalline CTFs within 20 minutes. Moreover, this method can be easily scaled up to  
499 produce a hundred grams of CTFs.<sup>130</sup> Notably, increased crystallinity led to a gradual narrowing  
500 of the bandgap of CTF and a shift of CB towards a more negative position. Subsequently, a  
501 scalable and eco-friendly method using polyphosphoric acid ( $\text{H}_6\text{P}_4\text{O}_{13}$ ) was developed by the  
502 same group, achieving superior crystallinity at the kilogram level.<sup>119</sup> The crystallinity of CTFs  
503 prepared from  $\text{H}_6\text{P}_4\text{O}_{13}$  was superior to that of CTFs prepared from analogs  $\text{P}_2\text{O}_5$  and  $\text{H}_3\text{PO}_4$ .<sup>123</sup>  
504 Experimental and DFT results demonstrated that  $\text{H}_6\text{P}_4\text{O}_{13}$  has a lower activation energy for the  
505 nitrile trimerization reaction.

506 The polycondensation method offers a solution to the challenges posed by super acids, as  
507 it not only avoids their strong corrosive nature but also allows for control over the nucleation  
508 rate during the reaction.<sup>18</sup> This method proves highly effective in improving the crystallinity of

509 CTFs. In a study, four CTF-HUST samples were synthesized using the condensation reaction  
510 between aldehydes and diamine hydrochloride, involving the formation of Schiff base and  
511 subsequent Michael addition, as shown in Figure 11.<sup>120</sup> The maximum photocatalytic hydrogen  
512 production rate of CTF-HUST in aqueous solution (TEOA as sacrificial agents) under visible  
513 light irradiation was obtained as  $2647 \mu\text{mol h}^{-1} \text{g}^{-1}$ . While the crystallinity of CTF-HUST was  
514 not optimal, the study suggests that controlled in situ oxidation of alcohols to form aldehyde  
515 monomers can significantly enhance the crystallinity of CTFs.<sup>131</sup> The strategy of alcohol in situ  
516 oxidation promoted the formation of low-density nuclei and crystal growth of CTF. This  
517 resulted in highly crystalline CTFs with enhanced visible light absorption up to approximately  
518 850 nm, leading to dramatically improved photocatalytic performance in hydrogen evolution  
519 compared to less crystalline or amorphous CTFs. The presence of defects in amorphous CTF  
520 structures contributes to the recombination of photogenerated electron-hole pairs, which  
521 hinders their photocatalytic activity. Additionally, researchers have successfully synthesized  
522 highly crystalline CTFs with tailored pore structures by controlling the monomer feeding rate  
523 to regulate nucleation and crystal growth.<sup>110</sup> In particular, under visible light illumination, the  
524 CTF-HUST-HC1 sample with exposed [001] crystal facets exhibited superior performance in  
525 the removal of nitric oxide (NO) compared to amorphous CTF-HUST-1 and even conventional  
526 g-C<sub>3</sub>N<sub>4</sub> photocatalysts. Nonetheless, the hydrophobic nature of CTFs, stemming from their  
527 aromatic backbone, limited their applicability in aqueous medium. To address this, specific  
528 functional groups were incorporated into the monomers to modulate the hydrophilicity of CTFs.  
529 The dominant role of the base reagent <sup>t</sup>BuOK in synthesizing CTFs with improved crystallinity  
530 and hydrophilicity using benzylamine-functionalized monomers has been highlighted.<sup>25</sup> The



531 crystallinity of CTFs was found to be enhanced with increasing strength of the base reagent.  
 532 The resulting CTF-HUST-A1 exhibited excellent performance in photocatalytic water splitting  
 533 reaction, utilizing  $\text{NiP}_x$  and Pt as cocatalysts without the need for sacrificial agents. In another  
 534 study, aniline and aromatic co-solvents were utilized as dual modulators to synthesize CTFs  
 535 with remarkable crystallinity.<sup>108</sup> The crystalline CTFs were regulated through peripheral  
 536 functionalization to enhance the oxidation of sulfides, achieving high conversion rates under  
 537 blue LED irradiation.



538

539 **Figure 11.** Rational synthesis of (a) CTF-HUST, (b) CTF-HUST-1, (c) CTF-HUST-2, (d) CTF-  
 540 HUST-3, and (e) CTF-HUST-4. The circles filled with different colors represent two types of  
 541 pores. HUST: Huazhong University of Science and Technology. (f) Photocatalytic H<sub>2</sub> evolution  
 542 rate of various CTF-HUSTs. (g) Photocatalytic H<sub>2</sub> evolution of CTF-HUST-1, CTF-HUST-2,  
 543 CTF-HUST-3 and CTF-HUST-4 and stability test for CTF-HUST-2 for running over 5 times.

544 The above photocatalytic experiments were done under visible light irradiation by using TEOA  
545 as sacrificial agents. Reproduced with permission from ref.<sup>120</sup>. Copyright 2017, John Wiley and  
546 sons.

547

548 From a crystallinity perspective, high crystallinity in semiconductors typically promotes  
549 efficient charge transfer from the center to the surface, leading to enhanced photocatalytic  
550 activity. However, it has been observed that low crystallinity can also enhance photocatalytic  
551 activity in certain inorganic semiconductors by providing active centers for photocatalytic  
552 reactions through the generation of shallow trapping sites such as impurities and vacancies.<sup>132</sup>,  
553 <sup>133</sup> Interestingly, similar observations have been made in the case of CTFs. It has been found  
554 that CTFs with low crystallinity sometimes exhibit better photocatalytic activity.<sup>134, 135</sup> The  
555 relationship between crystallinity and photocatalytic activity in CTFs is complex and  
556 multifaceted. It is possible that CTFs with different degrees of polymerization and crystallinity  
557 can form inherent electric fields between them, thereby improving the efficiency of charge  
558 carrier separation.

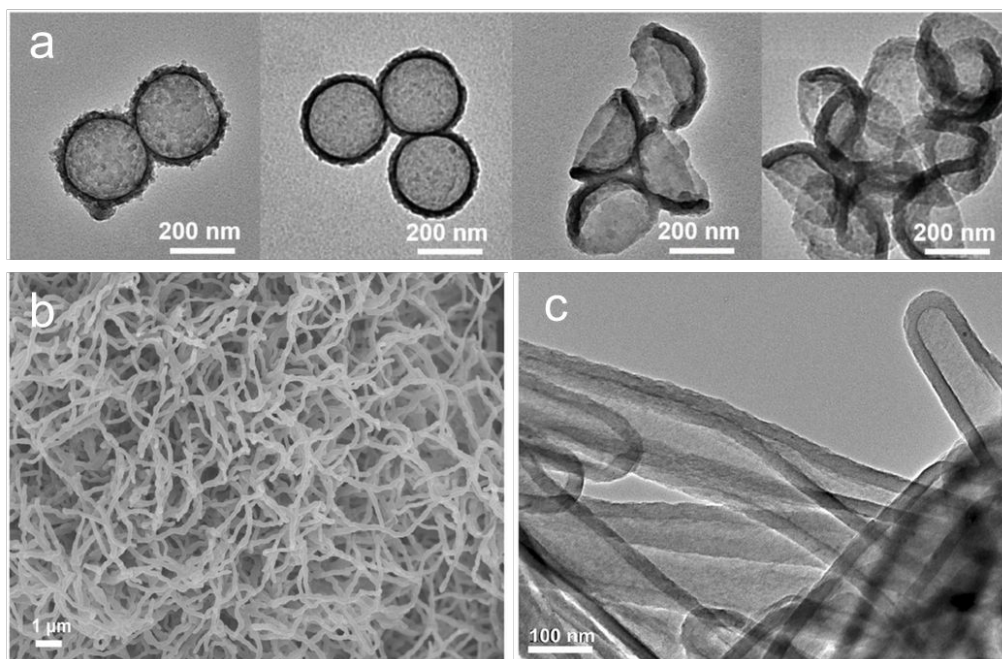
559

### 560 **3.2.2 Controlling morphology and thickness**

561 The control of CTF morphology and layers plays a crucial role in harnessing the benefits  
562 of quantum effects in various applications.<sup>111</sup> Hollow-structured CTFs (Figure 12a) with inner  
563 cavities and porous shells offer advantages such as efficient mass transfer of guest molecules  
564 and enhanced migration of photogenerated charges.<sup>136</sup> These hollow CTFs have demonstrated  
565 a four-fold improvement in the efficiency of HER reaction compared to bulk materials. To

566 synthesize CTFs with hollow spherical morphologies, silica nanospheres were employed as  
567 templates, resulting in CTFs (CTF-NS) with a shell thickness of approximately 10 nm and a  
568 large surface area, which exhibited efficient formation of H<sub>2</sub>O<sub>2</sub> from the O<sub>2</sub>-saturated aqueous  
569 solution.<sup>59</sup> Furthermore, the combination of mesoporous silica with thiophene-containing CTFs  
570 yielded a composite material with a hexagonal cylinder morphology, which was utilized for the  
571 photodegradation of dyes in water.<sup>96</sup> The hydrophilic nature and high surface area of silica  
572 enhanced the adsorption of organic molecules, expanding the application of CTFs as  
573 photocatalysts for water treatment. Similarly, the hollow nanoporous CTFs were synthesized  
574 using acid vapor-assisted solid-phase synthesis.<sup>137</sup> The photocatalytic performance for the  
575 photoreduction of 4-nitrophenol (4-NP) to 4-aminophenol (4-AP) was improved because the  
576 nanopores enhanced the mass transfer and light absorption. Additionally, olefin-linked CTFs  
577 (TTO-COF) nanotubes exhibited remarkable stability and performance in the selective  
578 oxidation of sulfides using O<sub>2</sub> under blue light.<sup>71</sup> These CTFs nanotubes, with a diameter of  
579 approximately 100 nm and a thickness of about 20 nm, provided spacious cavities and  
580 numerous reaction centers for organic transformations (Figure 12b and c).

581       When a photocatalyst is exposed to sunlight, the photogenerated carriers must effectively  
582 migrate from the bulk phase to the photocatalyst surface to participate in the reaction. Few-  
583 layer CTF nanosheets offer a solution to this challenge as they shorten the charge migrate  
584 distance to the solid-liquid interface and provide more exposed active sites compared to bulk  
585 materials. Two main strategies are commonly employed to obtain few-layer CTFs: exfoliation  
586 and bottom-up synthesis.<sup>138, 139</sup> Exfoliation, in particular, has garnered significant interest due  
587 to its unique advantage of directly producing nanosheets from bulk COFs.



588

589 **Figure 12.** (a) The transmission electron microscope (TEM) images of different etched CTFs.

590 Reproduced with permission from ref.<sup>136</sup>. Copyright 2019, John Wiley and sons. (b) SEM and

591 (c) TEM images of olefin-linked CTFs nanotubes. Reproduced with permission from ref.<sup>71</sup>.

592 Copyright 2021, Elsevier.

593

594 For instance, sulfuric acid was used as an intercalant and ammonium persulfate as an

595 oxidant to exfoliate bulk CTFs into ultrathin CTFs nanosheets.<sup>140</sup> This process resulted in

596 nanosheets with an extended visible light absorption edge up to 750 nm and a narrowed bandgap

597 from 2.82 eV (pristine-CTF) to 2.36 eV. Experimental and DFT calculations showed that the

598 conduction-band position of these ultrathin nanosheets was more favorable for promoting H<sub>2</sub>

599 evolution from water compared to that of bulk CTF under visible light irradiation. In another

600 study, researchers successfully prepared an ultrathin CTF nanosheet with a thickness of 1.5 nm

601 using a redox exfoliation process.<sup>88</sup> The resulting nanosheet exhibited distinct lamellar features

602 and smooth morphology after 30 drop-casting cycles and demonstrated a competitive H<sub>2</sub>

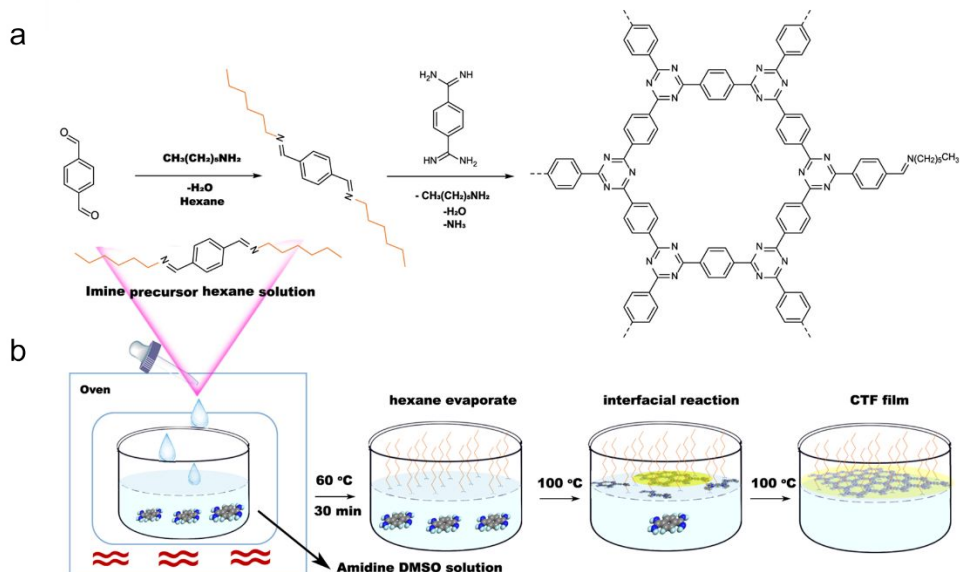
603 evolution rate of  $25.7 \text{ mmol h}^{-1} \text{ m}^{-2}$  among reported film devices.

604 Furthermore, a glycerol intercalation strategy was employed to exfoliate bulk CTFs into  
605 crystalline sheets (E-CTF-HC1).<sup>141</sup> The exfoliation process was found to be influenced by the  
606 vibrational states of glycerol molecules at different temperatures. N-doped quantum dots  
607 (CTFQDs) were obtained by exfoliating and cutting CTFs in piranha solution, resulting in a  
608 blue shift in the UV-vis spectra compared to bulk CTFs.<sup>142</sup> Ultrasonic assistance and  
609 grinding/ball milling have been widely used for the exfoliation of two-dimensional materials  
610 by overcoming interlayer interactions. For instance, Wang's group successfully prepared  
611 exfoliated CTFs<sup>143</sup> and fluorinated CTFs<sup>144</sup> nanosheets through mechanical milling processes.  
612 Micrometer-sized few-layer CTF sheets were obtained through micromechanical cleavage and  
613 liquid sonication.<sup>145</sup> However, CTF thin films prepared using these mechanical methods often  
614 exhibit lower crystallinity.

615 Bottom-up synthesis is another effective method for producing thin films of CTFs,  
616 allowing for large-area, controllable thickness films in a single step. One general approach to  
617 synthesize porous CTF membranes with intrinsic porosity involves catalyzing aromatic nitrile  
618 trimerization reactions at low temperatures using super acids. Dai<sup>117</sup> and Chung<sup>146</sup>, for example,  
619 have used  $\text{CF}_3\text{SO}_3\text{H}$  for in situ catalytic synthesis of CTF membranes on glass, although  
620 controlling the thickness, size, and crystallinity of these films can be challenging. Therefore,  
621 the two-phase interface synthesis method has been developed, which involves the trimerization  
622 of carbonitrile at the interface of  $\text{CH}_2\text{Cl}_2$  and  $\text{CF}_3\text{SO}_3\text{H}$  to synthesize single-layer/few-layer  
623 triazine-based two-dimensional polymers (2DP).<sup>147</sup> The high-resolution transmission electron  
624 microscopy (HR-TEM) images demonstrated the high structural order of these 2DPs.

625           Additionally, a mixture of 1,4-dicyanobenzene and  $\text{CH}_2\text{Cl}_2$  has been used to prepare few-  
626 layer 2D-CTF-1 nanosheets.<sup>148</sup> Wang et al. achieved the synthesis of single-layer CTF  
627 nanosheets with a thickness of approximately 1.1 nm through a combination of interface  
628 synthesis, mild oxidation, and ultrasonic-assisted exfoliation.<sup>149</sup> Moreover, Tan et al. developed  
629 an innovative organic solvent/air interfacial polymerization method to prepare large-area,  
630 thickness-controlled semicrystalline CTF films (Figure 13).<sup>122</sup> These films exhibited a high  
631 hydrogen evolution rate of  $5.4 \text{ mmol h}^{-1} \text{ m}^{-2}$ , attributed to their good light absorption, large  
632 lateral size, and crystal structure. In a recent development, monolayer-assisted surface-initiated  
633 Schiff-base-mediated aldol polycondensation was utilized to prepare large-area crystalline CTF  
634 films on various solid substrates.<sup>150</sup> The resulting films demonstrated lateral sizes of up to 120  
635  $\text{cm}^2$  and tunable thicknesses ranging from tens of nanometers to a few micrometers.

636           The low-dimensional structure and reduced particle size of CTF films serve to shorten the  
637 migration distance for photogenerated carriers while increasing the active sites on the surface.  
638 Both exfoliation and interfacial synthesis methods, which are commonly used, are effective for  
639 synthesizing CTF films. However, compared to exfoliation which produces thin films with  
640 small and inhomogeneous, interfacial synthesis is more favorable for producing large-area films  
641 with a controllable number of layers, offering the potential to design and prepare photocatalytic  
642 devices based on CTF films in the future.



643

644 **Figure 13.** (a) Rational synthesis of CTF. (b) Synthetic procedure for the fabrication of CTF

645 film on dimethyl sulfoxide (DMSO) surface assisted by imine precursor. Reproduced with

646 permission from ref.<sup>122</sup>. Copyright 2021, Springer Nature.

647

648 **3.2.3 Doping**

649 Chemical doping is a conventional and effective method to modify the electrical properties

650 of semiconductors, including the carrier concentration, Fermi energy level, and band

651 structure<sup>151, 152</sup>, thereby enhancing the limited visible light absorption and inefficient charge

652 separation of CTFs. Recent reports have demonstrated that the doping of halogen elements (F,

653 Cl and Br)<sup>153, 154</sup>, N<sup>155, 156</sup>, P<sup>157</sup>, and S<sup>158</sup> can modulate the electronic structure of CTF and

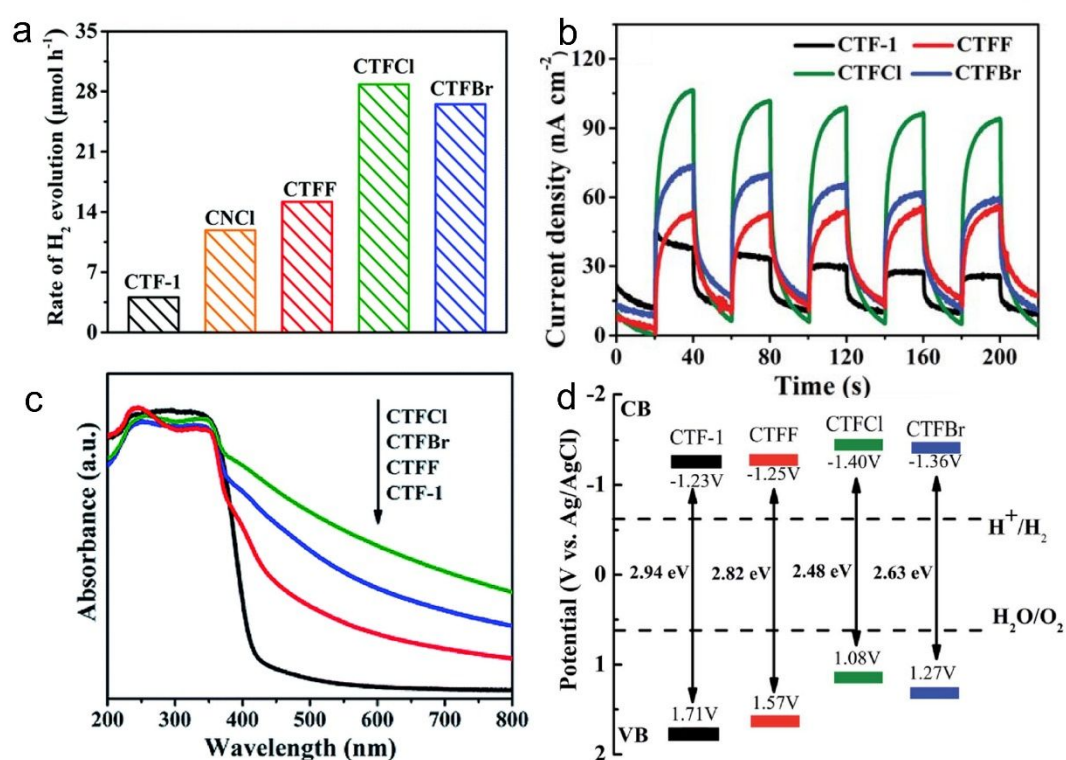
654 improve their photocatalytic activity.

655 For instance, the introduction of halogen elements through chemical doping has been

656 shown to significantly decrease the bandgap of CTFs.<sup>153</sup> Specifically, Cl doping resulted in a

657 narrower bandgap of 2.48 eV than pristine CTF (bandgap: 2.94 eV), leading to an

658 approximately 6.1 times increase in the H<sub>2</sub> evolution rate from water splitting (TEOA as  
 659 sacrificial agents) under visible light (Figure 14). This improvement can be attributed to the  
 660 more negative CB position of Cl-doped CTF, which facilitates more efficient charge transfer.  
 661 DFT and experimental results experimental analyses indicated that the formation of Cl-N and  
 662 Cl-C bonds in CTF promotes electronic delocalization and accelerates charge carrier  
 663 transportation.<sup>154</sup>



664  
 665 **Figure 14.** (a) Photocatalytic H<sub>2</sub> evolution rates over CTF-1, CNCl and CTFX (X = Cl, F, Br)  
 666 samples under visible light illumination by using TEOA as sacrificial agents. (b) Photocurrent  
 667 responses over CTF-1 and CTFX photoelectrodes under visible-light irradiation. (c) UV-vis  
 668 DRS spectra of CTF-1 and CTFX. (d) Electronic band structure of CTF-1 and the CTFX  
 669 samples (versus the saturated Ag/AgCl reference electrode at pH = 7). Reproduced with  
 670 permission from ref.<sup>153</sup>. Copyright 2019, Royal Society of Chemistry.



671 N-doped CTFs (T3N-CTF) have been achieved through Schiff-base condensation  
672 reactions using 5,5',5''-(1,3,5-triazine-2,4,6-triyl)tris(pyridine-2-amine) as the monomer.<sup>155</sup>  
673 Both triazine nitrogen and pyridine nitrogen have been identified as active sites in CTF. The  
674 incorporation of specific nitrogen atoms within the framework of T3N-CTF has shown  
675 improvements in light absorption, surface area expansion, and enhanced charge separation  
676 efficiency. Additionally, a simple hydrothermal treatment of CTF-1 with hydrazine hydrate has  
677 enabled the synthesis of self-doped nitrogen CTFs (NCTF-1).<sup>156</sup> NCTF-1 exhibited a CH<sub>4</sub>  
678 generation rate of 11.48 μmol g<sup>-1</sup> h<sup>-1</sup> in photocatalytic CO<sub>2</sub>RR, which was nine times higher  
679 than that of CTF-1. The excess nitrogen in NCTF-1 provided a CO<sub>2</sub>-friendly scaffold for  
680 selective adsorption and separation of CO<sub>2</sub>.

681 Similarly, P doping in CTF-1 promoted its hydrogen evolution performance, exhibiting a  
682 rate approximately 4.5 times higher than undoped CTF-1.<sup>157</sup> Moreover, P-doped CTF-1  
683 maintained high stability in H<sub>2</sub> evolution over a 20-hour cyclic reaction without significant  
684 changes in its crystal structure.

685 Furthermore, the introduction of a small amount of sulfur effectively altered the electronic  
686 properties and energy band structure of CTFs.<sup>158</sup> Photoelectric characterization studies revealed  
687 that S-doped CTFs exhibited a narrower bandgap, broader absorption edge, and reduced  
688 recombination of photogenerated carriers than bare CTF.

689 Doping other elements in organic semiconductor materials, especially in CTFs, is indeed  
690 more challenging compared to inorganic semiconductor materials. CTFs consist of carbon,  
691 hydrogen, nitrogen, and other non-metallic elements linked by covalent bonds, and doping  
692 often requires breaking the original covalent bond, which can damage the conjugated structure

693 and reduce the crystallinity of CTFs. Additionally, controlling the precise position of the doped  
694 atoms within the CTF structure is difficult. These challenges make the process of doping other  
695 elements in CTFs more complex and less controllable compared to inorganic semiconductors.

696

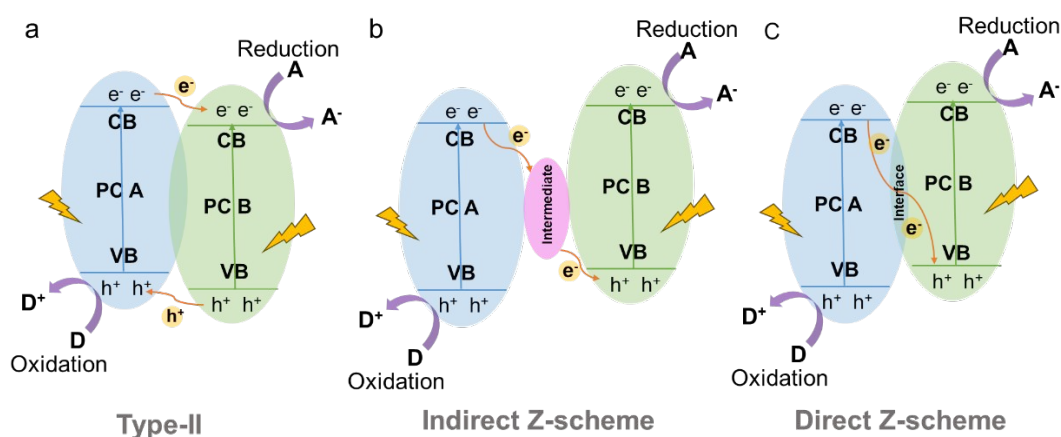
### 697 **3.3 Heterostructure**

#### 698 **3.3.1 Heterojunction**

699 The coupling of two semiconductors to form a heterojunction has proven to be an effective  
700 strategy for spatially separating photogenerated electron-hole pairs.<sup>159</sup> This is achieved by  
701 taking advantage of the different Fermi energy levels ( $E_F$ ) or work functions ( $W$ ) of the two  
702 semiconductors. As a result, a built-in electric field ( $E_D$ ) is established at the heterojunction  
703 interface, facilitating the movement of electrons from the semiconductor with a higher  $E_F$  to the  
704 one with a lower  $E_F$ .<sup>160</sup> This built-in electric field can promote the transfer of photogenerated  
705 carriers between the two semiconductors, reducing carrier recombination. Various types of  
706 semiconductor-semiconductor heterojunctions exist, including type-I (straddling gap), type-II  
707 (staggered gap), type-III (broken gap), Z-scheme, n-p, p-p, and n-n heterojunctions.<sup>161</sup> Among  
708 them, type-II<sup>162</sup> and Z-scheme<sup>163</sup> heterojunctions are commonly formed structures when  
709 combining CTFs with other semiconductor materials (Table 3).

710 In a type-II heterojunction (Figure 15a) between photocatalyst A (PC A) and photocatalyst  
711 B (PC B), electron and hole pairs are generated in both PC A and PC B upon illumination.<sup>164</sup>  
712 The electrons from PC A are transferred to PC B, while the holes move from PC B to PC A in  
713 the opposite direction. As a result, PC B accumulates electrons for reduction reactions and PC  
714 A accumulates holes for oxidation reactions. This spatial separation of charge carriers allows

715 for efficient reactions on each photocatalyst, enhancing overall photocatalytic performance. For  
 716 instance, the combination of CdS and CTF exhibited a photocatalytic H<sub>2</sub> production rate of  
 717 12150  $\mu\text{mol}\cdot\text{g}^{-1}\cdot\text{h}^{-1}$  from water under visible light irradiation, which was approximately 3 times  
 718 higher than that of pure CdS.<sup>165</sup> This enhanced performance can be attributed to the strong  
 719 interaction and matched band potentials between CdS and CTF, which facilitated the  
 720 delocalization of photogenerated carriers out of the CTF plane and effectively suppressed the  
 721 photocorrosion of CdS induced by photogenerated holes. Additionally, CTF served not only as  
 722 a supporter but also as a photocatalyst and an electron donor within the composite structure.<sup>166</sup>  
 723



724 **Figure 15.** Schematic illustration of the electron-transfer route in a combined system using two  
 725 kinds of semiconductors with (a) type-II (b) indirect Z-scheme (c) direct Z-scheme  
 726 heterojunction.  
 727

728  
 729 The Z-scheme heterojunction consists of two semiconductors with a similar band structure  
 730 to that of the type-II heterojunction, but with different electron-hole transfer paths, as shown in  
 731 Figure 15.<sup>167</sup> In the Z-scheme heterojunction, the electrons from the CB of PC A combine and  
 732 annihilate with the holes from the VB of PC B through either a suitable intermediate (indirect

733 Z-scheme heterostructure) (Figure 15b) or direct contact interface (direct Z-scheme  
734 heterostructure) (Figure 15c).<sup>168</sup> This arrangement leads to a spatial separation of electrons and  
735 holes, with electrons accumulating in the CB of PC B and holes accumulating in the VB of PC  
736 A, leading to a higher redox capability.

737 For example, the coupling of CdS and CTF-1 in a membrane configuration exhibited  
738 outstanding photocatalytic sterilization effects in photocatalytic in situ cleaning and  
739 disinfection due to the generation of abundant hole pairs as well as reactive oxygen species,  
740 solving the stubborn fouling problems of 2D membranes.<sup>169</sup> In addition, a Z-scheme  
741 SnS<sub>2</sub>/sulfur-bridged CTFs (S-CTFs) photocatalyst (SnS<sub>2</sub>/S-CTFs) was developed, exhibiting  
742 efficient CO<sub>2</sub> adsorption due to the CO<sub>2</sub>-friendly nature of S-CTFs and promoting efficient  
743 separation of photogenerated carriers. Such SnS<sub>2</sub>/S-CTFs exhibited exceptional visible-light-  
744 driven CO<sub>2</sub> photoreduction activity, generating CO and CH<sub>4</sub>.<sup>170</sup> ZnIn<sub>2</sub>S<sub>4</sub> (ZIS) is a sulfide  
745 photocatalyst with a tunable bandgap (2.06-2.85 eV).<sup>171</sup> Despite its high photogenerated  
746 electron efficiency, the recombination of photogenerated carriers remains an issue. By  
747 constructing a Z-scheme heterojunction between porphyrin-based CTF and ZIS, effective  
748 charge separation was achieved. Experimental and theoretical calculations demonstrated that  
749 photogenerated electrons were transferred via the Z-scheme route, overcoming the speed-  
750 limiting step in photocatalytic hydrogen evolution.

751 Due to their excellent optical properties and electronic conductivity, 2D materials such as  
752 carbon nitride (C<sub>3</sub>N<sub>4</sub>) and black phosphorus (BP) nanosheets have been extensively explored  
753 to form heterojunction with CTF and enhance the visible light absorption and charge transfer  
754 properties of CTF-based photocatalysts.<sup>172-174</sup> For instance, integration of 2D C<sub>3</sub>N<sub>4</sub> with CTF

755 resulted in a metal-free heterostructure with a type I band alignment, facilitating efficient charge  
756 migration. The hybrid material exhibited remarkable stability and high selectivity for  
757 photocatalytic CO<sub>2</sub>RR to produce CO during 3 cyclic runs in 30 h by using [Co(bpy)<sub>3</sub>]<sup>2+</sup> as the  
758 cocatalysts.<sup>172</sup> Similarly, the incorporation of BP nanosheets into CTF enabled highly active  
759 photocatalytic H<sub>2</sub> evolution at a rate of 17.1 mmol·h<sup>-1</sup>·g<sup>-1</sup> in water (formaldehyde as sacrificial  
760 agents) under 300 W Xenon lamp with full spectrum.<sup>173</sup> The crucial P-C bonding at the interface  
761 promoted electron transfer, while the accumulation of electrons on BP nanosheets prevented  
762 surface oxidation. Furthermore, a sandwich-type CTF-BP-Pt photocatalyst was fabricated by  
763 depositing Pt on BP, forming a bridge joint with Pt(δ<sup>+</sup>)-P(δ<sup>-</sup>)-N(δ<sup>+</sup>) surface bonding states,  
764 enabling efficient charge separation and extending the light absorption range of the hybrid  
765 material.<sup>175</sup> A type II heterojunction was also constructed using triphenylphosphine-based COF  
766 (P-COF) and CTF.<sup>176</sup> The interaction between P-COF and CTF expanded the visible spectrum  
767 utilization and facilitated the transfer of photogenerated carriers, resulting in a hydrogen  
768 production rate approximately 2.5 times higher than that of pristine CTF.

769 Metal-organic frameworks (MOFs) have been extensively applied in photocatalytic fields  
770 due to their electrical conductivities and manifold building structure. Similar to porous  
771 crystalline materials, MOF can be well integrated with CTF to fabricate hybrid materials with  
772 rapid charge transfer and good stability. For instance, in the case of NH<sub>2</sub>-UiO-66 (Zr), the  
773 dissolution of the link between the carboxyl in 2-aminoterephthalic acid and Zr<sup>2+</sup> of NH<sub>2</sub>-UiO-  
774 66 (Zr) in alkaline environments limits its practical application as a photocatalyst. To overcome  
775 this issue, CTF was anchored on the surface of NH<sub>2</sub>-UiO-66 (Zr) to slow down its  
776 decomposition. The resulting hybrid material (NH<sub>2</sub>-UiO-66/CTF-3wt% Pt) demonstrated a

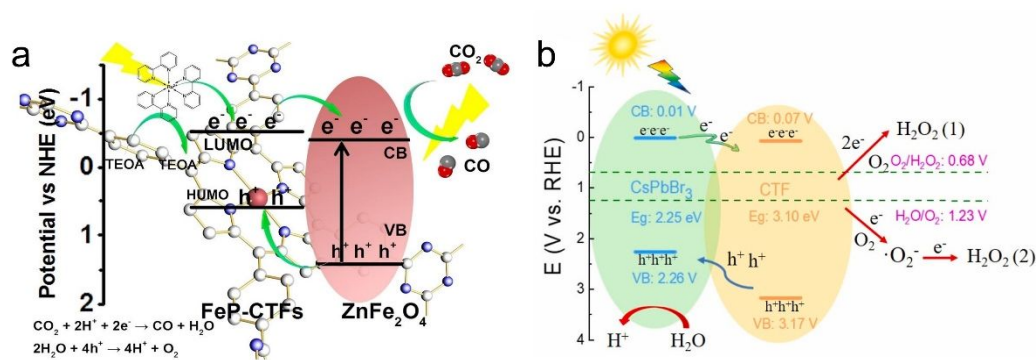
777 hydrogen production rate of  $8.44 \text{ mmol} \cdot \text{h}^{-1} \cdot \text{g}^{-1}$  in alkaline aqueous solution (TEOA as sacrificial  
778 agents) under 300 W Xe lamp (400 nm cutoff filter) and could be recycled up to 10 times with  
779 consistent performance.<sup>177</sup> As another example, a conductive 2D MOF (Ni-CAT-1) was tightly  
780 grafted onto CTF to create a Z-scheme heterostructure through a unique coordinating  
781 connection between the dual N sites of the CTF terminal amidine groups and Ni ions of Ni-  
782 CAT-1.<sup>178</sup> The transient photocurrent density of Ni-CAT-1/CTF-1 was more than twice as high  
783 as that of pure Ni-CAT-1 and CTF-1, indicating the superior separation and migration ability  
784 of the composite. The hybrid material also exhibited high activity for  $\text{H}_2$  evolution under visible  
785 light.

786 Metal oxide semiconductors such as  $\text{TiO}_2$ ,  $\text{CuCo}_2\text{O}_4$  and  $\text{ZnFe}_2\text{O}_4$  have been successfully  
787 combined with CTF to fabricate organic-inorganic hybrid materials for photocatalytic solar fuel  
788 production.<sup>167, 179-181</sup> As an example, the  $\text{Au}@\text{TiO}_2\text{-X}\%\text{TrTh}$  Z-scheme heterojunction,  
789 comprising CTF-based TrTh,  $\text{TiO}_2$ , and Au nanoparticles, demonstrated high activity for  
790 photocatalytic hydrogen production in aqueous solution (TEOA as sacrificial agents) under  
791 visible light irradiation.<sup>179</sup> This was attributed to the synergetic effect of the localized surface  
792 plasmon resonance of Au nanoparticles and the Z-scheme electron transfer pathway for  
793 photogenerated carriers. Additionally,  $\text{Co}^{2+}$ -immobilized Pyridine CTF (CTF-Py) decorated on  
794  $\text{NH}_2^-$  functionalized  $\text{TiO}_2$  ( $\text{NH}_2\text{-TiO}_2$ ) surface enabled the conversion of  $\text{CO}_2$  into CO using  
795  $\text{H}_2\text{O}$  as the electron donor without the need for additional sacrificial agents.<sup>180</sup> The excited  
796 electrons transfer from  $\text{TiO}_2$  to CTF-Py, accumulating at the metal sites on the hybrid material  
797 surface for reducing  $\text{CO}_2$ , while the holes concentrate on the  $\text{TiO}_2$  surface for  $\text{H}_2\text{O}$  oxidation.  
798 The formation of a Z-scheme heterojunction between the staggered band structures of  $\text{TiO}_2$  and

799 CTF-Py facilitated electron-hole separation and photoinduced charge transfer. Defect TiO<sub>2</sub>  
800 anchored on CTF through a well-defined chemical bonding between the amine group of CTF  
801 and Ti<sup>3+</sup> also achieved efficient photocatalytic CO<sub>2</sub> conversion.<sup>182</sup> The large surface area of  
802 CTF provided rich adsorption sites for CO<sub>2</sub>, and the Ti-N facilitated the selective conversion of  
803 CO<sub>2</sub> into CO with a selectivity of approximately 100%. Similarly, the direct Z-scheme  
804 heterojunction between p-type semiconductor CuCo<sub>2</sub>O<sub>4</sub> and CTF-1 allowed for the efficient  
805 photocatalytic conversion of CO<sub>2</sub> into CO. Electron spin resonance (ESR) analysis revealed  
806 that photogenerated holes tended to accumulate in the valence band of CuCo<sub>2</sub>O<sub>4</sub>, while  
807 electrons transferred to the conduction band of CTF-1, achieving spatial separation of electrons  
808 and holes.<sup>167</sup> ZnFe<sub>2</sub>O<sub>4</sub> is a promising visible-light-responsive photocatalyst due to its narrow  
809 bandgap while being resistant to photochemical corrosion. When ZnFe<sub>2</sub>O<sub>4</sub> was combined with  
810 CTF, the band gap energy of CTF-1 was reduced, resulting in a broadened range of visible light  
811 absorption. Therefore, the obtained ZnFe<sub>2</sub>O<sub>4</sub>/CTF exhibited excellent performance in the  
812 photocatalytic degradation of methylene blue (MB).<sup>181</sup> In comparison to ZnFe<sub>2</sub>O<sub>4</sub>/CTF,  
813 ZnFe<sub>2</sub>O<sub>4</sub>/FeP-CTF exhibited a higher exposure of (311) crystal planes and a larger surface area,  
814 which facilitated closer contact between CO<sub>2</sub> and the active sites. The strong interaction  
815 between ZnFe<sub>2</sub>O<sub>4</sub> and FeP-CTF enhanced interfacial charge transfer and separation, thereby  
816 leading to improved reaction performance in photocatalytic CO<sub>2</sub> reduction (Figure 16a).<sup>183</sup>

817 Metal halide perovskites are well-known for their promising photocatalytic properties,  
818 characterized by their high molar extinction coefficients and tunable light absorption.<sup>184</sup> In a  
819 study, CsPbBr<sub>3</sub> quantum dots (QDs) were immobilized on CTF-1 for photocatalytic CO<sub>2</sub>  
820 reduction to CO, resulting in an AQY of over 0.07% at 450 nm. CTF-1 acted as a suitable

821 support with abundant cavities for adsorbing and activating  $\text{CO}_2$ , while also enhancing the  
 822 charge transfer ability of  $\text{CsPbBr}_3$  QDs.<sup>185</sup> Similarly,  $\text{CsPbBr}_3/\text{CTFs}$  demonstrated excellent  
 823 performance in photocatalytic  $\text{H}_2\text{O}_2$  production. The photogenerated holes oxidize  $\text{H}_2\text{O}$  to  
 824 produce hydrogen  $\text{H}^+$ , while the electrons migrate from  $\text{CsPbBr}_3$  to the surface of CTF to react  
 825 with adsorbed  $\text{O}_2$  to produce  $\text{H}_2\text{O}_2$  via a one-step two-electron reaction pathway and two-step  
 826 one-electron reaction path (Figure 16b).<sup>186</sup>



827

828 **Figure 16.** The proposed charge transfer mechanisms: (a)  $\text{ZnFe}_2\text{O}_4/\text{FeP-CTF}$  for the  
 829 photocatalytic  $\text{CO}_2$  reduction system. Reproduced with permission from ref.<sup>183</sup>. Copyright 2021,  
 830 Elsevier. (b)  $\text{CsPbBr}_3/\text{CTF-2}$  for photocatalytic  $\text{H}_2\text{O}_2$  production. Reproduced with permission  
 831 from ref.<sup>186</sup>. Copyright 2022, Elsevier.

832

833 The design concept of heterojunction materials has been widely utilized in photocatalysis,  
 834 facilitated by the built-in electric field in the heterojunction that drives the separation of  
 835 photogenerated electrons and holes. By selecting semiconductor materials with matching  
 836 energy band structure and Fermi energy level to CTFs, the efficiency of photogenerated carrier  
 837 separation and migration can be significantly improved, thereby enhancing photocatalytic  
 838 performance. While CTFs and organic semiconductors can often be effectively contacted  
 839 through interactions like  $\pi$ - $\pi$  and electrostatic adsorption, achieving effective contact with



840 inorganic semiconductors poses a challenge. In many cases, the electrostatic adsorption  
 841 between CTFs and inorganic semiconductors cannot overcome the density difference, resulting  
 842 in separation and the inability to fully exploit the benefits of a heterojunction structure in the  
 843 photocatalytic reaction. However, it has been reported that modifying the surface of the  
 844 inorganic semiconductor can facilitate the formation of covalent bonds with CTFs, enhancing  
 845 the contact force and offering insights for future design on the composites of CTFs and  
 846 inorganic materials.

847

848 **Table 3.** Summary of the photocatalytic performance of photocatalysts based on CTFs with  
 849 various heterojunctions.

Heterojunction	Photocatalyst	Reaction	Reactants	Light source	Production	Ref
type-II	20 mg CdS	HER	H <sub>2</sub> O+LA <sup>a</sup>	300 W Xe lamp	12150 μmol·h <sup>-1</sup> ·g <sup>-1</sup>	165
	NPs/3% CTF-1			(λ > 420 nm)		
	1 wt% Pt					
	20 mg 20% CdS-	HER	H <sub>2</sub> O+LA	300 W Xe lamp	11430 μmol·h <sup>-1</sup> ·g <sup>-1</sup>	166
	CTF-1			(λ > 420 nm)	AQY <sup>c</sup> =16.3% 420 nm	
	1 wt% Pt					
	10 mg NH <sub>2</sub> -UiO-	HER	H <sub>2</sub> O+ TEOA <sup>b</sup>	300 W Xe lamp	8440 μmol·h <sup>-1</sup> ·g <sup>-1</sup>	177
	66/COF			(λ > 400 nm)		
	3 wt% Pt					
Z-scheme	10 mg 5 wt%CuCo <sub>2</sub> O <sub>4</sub> /CT	CO <sub>2</sub> RR	H <sub>2</sub> O+TEOA + MeCN <sup>c</sup>	300 W Xe lamp	14.9 μmol·h <sup>-1</sup> ·g <sup>-1</sup> CO	167
				(λ > 420 nm)		

---

F-1								
7.0	mg							
[Ru(bpy) <sub>3</sub> ]Cl <sub>2</sub> ·6H <sub>2</sub> O								
50	mg	COP-	HER	H <sub>2</sub> O+Na <sub>2</sub> S+N	300 W Xe lamp	5040 μmol·h <sup>-1</sup> ·g <sup>-1</sup>		171
ZnIn <sub>2</sub> S <sub>4</sub>				a <sub>2</sub> SO <sub>3</sub>				
1 wt% Pt								
50	mg	Au@TiO <sub>2</sub> -	HER	H <sub>2</sub> O+TEOA	300 W Xe lamp	4288.54 μmol·h <sup>-1</sup> ·g <sup>-1</sup>		179
12%TrTh					(λ > 420 nm)			
3% Pt								
15	mg	60-	CO <sub>2</sub> RR	H <sub>2</sub> O	300 W Xe lamp	CO selectivity: 98.3%		180
TiO <sub>2</sub> @CTF-Py					(λ > 320 nm)	43.34 μmol·h <sup>-1</sup> ·g <sup>-1</sup> CO		
0.045 mM CoCl <sub>2</sub>								
NCTS-2			CO <sub>2</sub> RR	MeCN+AA <sup>d</sup>	300 W Xe lamp	CO selectivity:100%		182
						7.51 μmol CO after 4h		
						AQY=6.81% 365 nm		
20	mg	SnS <sub>2</sub> /S-	CO <sub>2</sub> RR	TEOA+H <sub>2</sub> O	300 W Xe lamp	123.6 μmol·h <sup>-1</sup> ·g <sup>-1</sup> CO		187
CTFs					(λ > 420 nm)	43.4 μmol·h <sup>-1</sup> ·g <sup>-1</sup> CH <sub>4</sub>		

---

850 <sup>a</sup> LA: lactic acid, <sup>b</sup> TEOA: triethanolamine, <sup>c</sup> MeCN: acetonitrile, <sup>d</sup> AA: ascorbic acid, <sup>e</sup> AQY: apparent quantum

851 yield

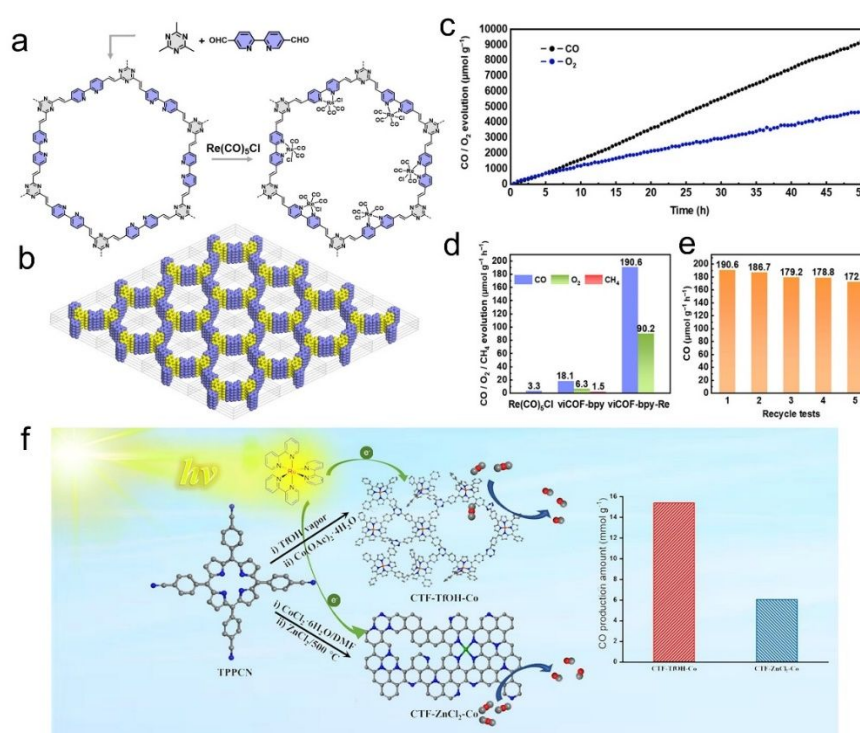
852

853 **3.3.2 Single-atom**

854 Single-atom catalysts exhibit exceptionally high site-specific activity compared to sub-  
855 nanoscale and microscale nanoparticles, attributed to their maximized atomic utilization  
856 (~100%). Moreover, they can be anchored onto the surface of photocatalysts to effectively  
857 promote the separation of photogenerated electron-hole pairs.<sup>188-191</sup> However, single-atom  
858 catalysts tend to aggregate due to their high surface free energy, resulting in a decrease in  
859 catalytic activities. To address this issue, CTF with nitrogen-rich properties has been applied to  
860 serve as a promising support to improve the dispersibility and stability of single-atom catalysts.  
861 In recent years, various kinds of single atoms (such as Pt<sup>188, 192</sup>, Fe<sup>193</sup>, Ni<sup>194, 195</sup>, Pd<sup>196</sup>, Ir<sup>197</sup>, Cu<sup>189,</sup>  
862 <sup>198</sup>, Co<sup>191, 199</sup>, Ti<sup>200</sup>, and more) have been anchored on CTF for various photocatalytic  
863 applications. For instance, by constructing CTFs with -N<sub>3</sub> sites, Pt single-atom catalysts have  
864 been loaded for photocatalytic N<sub>2</sub> fixation, achieving an ammonia production rate of up to  
865 171.40 μmol g<sup>-1</sup> h<sup>-1</sup> was achieved.<sup>192</sup> High-angle annular dark-field scanning transmission  
866 electron microscopy (HAADF-STEM) and extended X-ray absorption fine structure (EXAFS)  
867 analysis confirmed the presence of the active center Pt-N<sub>3</sub> structure. The introduction of Fe<sup>3+</sup>  
868 into the CTFs modified the optical adsorption and improved the conductivity and charge  
869 transfer rate of the CTFs without destroying their layered structure. Therefore, Fe-CTFs  
870 exhibited a 28-fold enhanced H<sub>2</sub> evolution rate from water splitting compared to the pristine  
871 CTFs.<sup>193</sup> Bipyridine is one of the most common ligands in complex catalysts, and its  
872 introduction into the CTF backbone provides an effective active site for coordination with  
873 transition metals. The bipyridine-based CTF-loaded single-atom catalysts such as Pd,<sup>196</sup> Ir<sup>197</sup>  
874 have demonstrated good catalytic performance in photocatalytic hydrogen production from  
875 water in the presence of an electron donor.

876 Cu,<sup>189</sup> Co,<sup>191,201</sup> Ru<sup>202</sup> and Re<sup>203</sup> are of great interest for their considerable catalytic activity  
877 in photocatalytic CO<sub>2</sub>RR. As an example, Cu single atoms confined into CTF-1 effectively  
878 enhanced the visible light absorption and the CO<sub>2</sub> adsorption capacity of CTF-1, with a  
879 production selectivity of CH<sub>4</sub> over 98.31% in photocatalytic CO<sub>2</sub>RR.<sup>189</sup> DFT calculations  
880 confirmed the synergic effect of the single atom metal sites and CTF host, reducing the reaction  
881 energy barriers for forming \*COOH intermediates and accelerating CO<sub>2</sub> adsorption and  
882 desorption of produced gas.<sup>190</sup> In-situ diffuse reflectance infrared Fourier transform  
883 spectroscopy (DRIFTS) assisted with DFT demonstrated that the transition of \*COOH to \*CO  
884 species is more thermodynamically favorable on Fe single atoms/CTF surface compared with  
885 pure CTF surface. Moreover, the specific atomic-level interaction is more inclined to dissociate  
886 \*CO into CO instead of further CO\* protonation to CHO\* and therefore exhibited high  
887 selectivity of CO in the CO<sub>2</sub> reduction process. CTFs confining Co single atoms were used for  
888 efficient CO<sub>2</sub>RR and H<sub>2</sub> production, enabling an efficiency far surpassing those of Co  
889 nanoparticles/CTF and pure CTF.<sup>204</sup> Numerous literature results indicate that metal ions  
890 anchored on bipyridyl and porphyrin-based COFs improve the CO<sub>2</sub> photoreduction  
891 performance.<sup>205-207</sup> The bipyridyl-CTF coordinated with Ru<sup>202</sup> and Re<sup>203</sup> single atoms showed  
892 good activity in the photocatalytic CO<sub>2</sub>RR to form formate and CO, respectively, with a formate  
893 production rate of 2090 μmol g<sup>-1</sup> h<sup>-1</sup>, and a turnover number (TON) of 4.8 for CO<sub>2</sub>-to-CO  
894 conversion. Recently, the fully conjugated viCOF-bpy-Re was synthesized through an Aldol  
895 condensation reaction by incorporating rhenium complex and triazine ring structures (Figure  
896 17a and b). viCOF-bpy-Re exhibited an outstanding performance for converting CO<sub>2</sub> into CO  
897 under visible light by using H<sub>2</sub>O as sacrificial agents (Figure 17c, d and e).<sup>208</sup> DFT results

898 further revealed the excited intramolecular charge transfer process from the triazine ring unit  
 899 to the Re-bipyridine complex. As another example, Co-porphyrin-based CTF was synthesized  
 900 under mild conditions to preserve the structure of porphyrin units, showing good charge  
 901 separation ability in photoluminescence spectra.<sup>209</sup> Additionally, the high N content of CTFs  
 902 endowed this catalyst with a strong CO<sub>2</sub> adsorption capacity, exhibiting better activity in  
 903 photocatalytic CO<sub>2</sub>RR with a CO yield of 2562.8 μmol g<sup>-1</sup> h<sup>-1</sup> (Figure 17f).



904  
 905 **Figure 17.** (a) The synthesis of viCOF-bpy and viCOF-bpy-Re. (b) Diagram of the alternating  
 906 arrangement of bipyridine and triazine ring units. (c) Time-dependent CO and O<sub>2</sub> production  
 907 performance of viCOF-bpy-Re. (d) Photocatalytic CO<sub>2</sub> reduction performance of Re-complex,  
 908 viCOF-bpy, and viCOF-bpy-Re. (e) Stability tests of viCOF-bpy-Re. Reproduced with  
 909 permission from ref.<sup>208</sup>. Copyright 2023, John Wiley and Sons. (f) Porphyrin-based CTFs for  
 910 photocatalytic CO<sub>2</sub> reduction. Reproduced with permission from ref.<sup>209</sup>. Copyright 2023,  
 911 Elsevier.

912

913         Single-atom catalyst-loaded CTFs fully harness the catalytic ability of metal atoms, with  
914 their ultra-high atom utilization enhancing photocatalytic performance and reducing the amount  
915 of precious metal required. However, to maximize the catalytic performance of metal atoms, it  
916 is essential to consider the introduction of effective ligand units into the structure of CTFs.

917

### 918 **3.3.3 Composite structures**

919         CTFs are considered promising supports for photocatalytic applications due to their large  
920 surface areas and well-defined nitrogen sites. These unique properties enable CTFs to form  
921 strong nitrogen-metal interactions, which allows for the integration of other materials to  
922 establish composite structures with enhanced performance.<sup>210</sup>

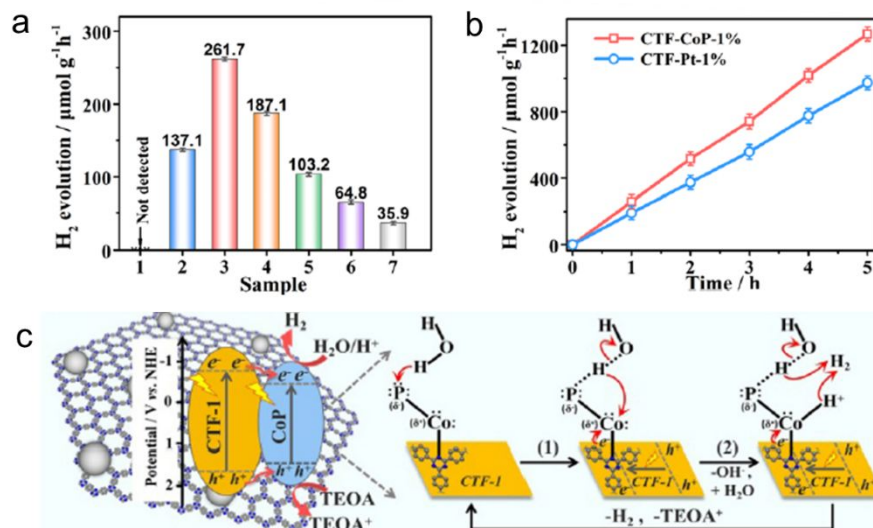
923         Transition metal phosphides (TMPs) have gained significant attention in the field of  
924 photocatalysis due to their exceptional electrical conductivity, cost-effectiveness, and versatile  
925 composition. For instance, Ni<sub>2</sub>P alloys have shown excellent performance in photocatalytic H<sub>2</sub>  
926 evolution from water, making them a potential alternative to Pt as a cocatalyst.<sup>211</sup> Previous  
927 studies have confirmed that 2.8wt% Ni<sub>2</sub>P alloys-CTF demonstrated comparable H<sub>2</sub> evolution  
928 rates (5.84 mmol h<sup>-1</sup> g<sup>-1</sup>) to 3.0wt% Pt/CTF (~6.1 mmol h<sup>-1</sup> g<sup>-1</sup>) under visible light irradiation.<sup>212</sup>  
929 Similarly, Co<sub>2</sub>P nanocrystals anchored on CTFs using a simple phosphidation strategy resulted  
930 in a P-CTF-Co<sub>2</sub>P photocatalyst, which exhibited outstanding photocatalytic H<sub>2</sub> evolution  
931 activity (7.6 mmol h<sup>-1</sup> g<sup>-1</sup>) among CTF-based hybrid materials with non-platinum cocatalysts.  
932 <sup>213</sup> Co<sub>2</sub>P accumulated rich electrons via the interfacial P-C bonds for reducing protons to  
933 produce H<sub>2</sub>. Further investigations have revealed that the P<sup>δ-</sup>-Co<sup>δ+</sup>-N<sup>δ-</sup> state in the CTF/CoP

934 complex induced by the polarization effect of the N site facilitated the adsorption and  
935 dissociation of H<sub>2</sub>O, as shown in Figure 18.<sup>214</sup>

936 Carbon materials such as carbon quantum dots (CQDs), carbon nanotubes (CNT), and  
937 graphene oxide (GO) have found widespread use in various fields, including photocatalysis,  
938 electrocatalysis, sensing, and bioimaging, attributable to their unique photoelectric properties,  
939 quantum confinement effects, high photochemical stability, and environmentally friendly  
940 nature.<sup>215-217</sup> In the study of CQDs/CTFs for photocatalytic hydrogen evolution from water,  
941 photoelectrochemical characterizations revealed that the introduction of CQDs not only  
942 extended the visible light response range but also served as an electron storage, with the light  
943 emitted in its multiphoton active process being captured by CTF-1 to enhance the separation of  
944 photogenerated electron-hole pairs.<sup>218</sup> Moreover, when CTF was combined with the electronic  
945 conductivity mediator CNT, the Schottky barrier was reduced, which facilitated the transfer of  
946 photogenerated charges from the CTF bulk to the surface catalytical active sites, resulting in an  
947 almost complete reduction of Cr(VI) under visible light irradiation for 2 hours.<sup>219</sup> Additionally,  
948 the combination of  $\pi$ -conjugation-linked CTF-1 with GO was found to boost photocatalytic H<sub>2</sub>  
949 evolution, with GO enhancing the hydrogen production efficiency of CTF by nine times at a  
950 content of 3% under visible light irradiation through the  $\pi$ -conjugate effect between them.<sup>217</sup>  
951 The uniformed GO thin layer not only acted as an electron transport "bridge" to facilitate the  
952 separation of photogenerated charges but also shortened the distance of electron migration.

953 The research on replacing precious metals and other co-catalysts represents a highly  
954 practical and significant endeavor. The investigation of the composite structure of CTFs, as  
955 mentioned earlier, has instilled confidence in the potential replacement of precious metal co-

956 catalysts like Pt and Rh with non-precious metal compounds. These studies offer crucial  
 957 experimental data to support the quest for cost-effective and efficient co-catalysts for hydrogen  
 958 and oxygen evolution reactions.



959  
 960 **Figure 18.** (a) Photocatalytic H<sub>2</sub> evolution over (1) CTF-1 or CoP, CTF-CoP photocatalysts  
 961 with different contents of CoP: (2) 0.5%, (3) 1%, (4) 3%, and (5) 5%, (6) physically  
 962 immobilized CTF/CoP-1% and (7) physical mixed CTF-1 + CoP-1%. (b) Photocatalytic H<sub>2</sub>  
 963 evolution rate over CTF-CoP-1% and CoP-Pt-1%. (c) The possible mechanism of charge  
 964 transfer over the obtained CTF-CoP-1% for photocatalytic H<sub>2</sub> evolution. The above  
 965 experiments were done under visible light irradiation by using TEOA as sacrificial agents.  
 966 Reproduced with permission from ref.<sup>214</sup>. Copyright 2022, Royal Society of Chemistry.

967

#### 968 4. Conclusions and perspectives

969 CTFs possess triazine ring structures with a robust conjugated system, ample nitrogen  
 970 content, exceptional visible light absorption, high chemical stability, substantial specific



971 surface area, and versatile modifiability. These outstanding properties render CTFs highly  
972 advantageous for photocatalytic hydrogen and oxygen evolution from water in the presence of  
973 sacrificial reagents, overall water splitting, CO<sub>2</sub> reduction, and organic reactions. Nonetheless,  
974 CTFs do exhibit certain defects and boundaries that hinder the transmission of photogenerated  
975 electrons, leading to suboptimal separation efficiency of photogenerated carriers and significant  
976 electron-hole recombination.

977 This review highlights various strategies to overcome these challenges and enhance the  
978 photocatalytic performance of CTFs (Table 4). By designing and constructing new types of  
979 CTFs, such as by introducing organic functional groups and leveraging the synergistic effect  
980 between functional groups and triazine rings, the intrinsic photoelectric properties of CTFs,  
981 such as bandgap, photogenerated carrier separation, and recombination efficiency, can be  
982 regulated. In addition, the D-A theory serves as a valuable tool for designing and synthesizing  
983 high-performance photocatalytic materials. The conjugation system in the D-A structure, with  
984 different electron affinity and ionization energy between the donor and acceptor, broadens the  
985 visible light absorption range and facilitates the transfer of photogenerated electrons from the  
986 donor to the acceptor. This acceleration of photogenerated electron-hole pair separation  
987 increases the electron transport rate within the molecule and reduces the recombination sites  
988 for electrons and holes.

989

990 **Table 4.** Summary of how the developed strategies impact specific processes within  
991 photocatalysis using CTF-based materials.

---

Strategy	Absorption of photons	Charge migration	Surface reaction
----------	-----------------------	------------------	------------------

---

Introducing functional groups	√	√	
Donor-Acceptor	√	√	
Improving crystallinity	√	√	
Morphology and thickness	√	√	
Doping	√	√	√
Heterojunction		√	√
Single-atom			√
Composite structures		√	√

992

993       The high crystallinity of semiconductor materials contributes to fewer defects, which in  
994 turn reduces the recombination sites for electrons and holes. However, during the synthesis of  
995 CTFs, poorly reversible self-healing often results in unsatisfactory crystallinity, particularly for  
996 non-imine bonded CTFs. To address this issue, several synthesis methods have been developed,  
997 including ionothermal, superacid-catalyzed, polycondensation, polyphosphoric acid-catalyzed,  
998 and microwave-assisted methods. Among these, microwave-assisted synthesis and  
999 polyphosphoric acid methods have shown potential for large-scale synthesis of high  
1000 crystallinity CTFs. Photocatalytic reactions rely on the efficient migration of photogenerated  
1001 electrons to the surface of semiconductors. However, CTFs tend to stack up and form bulk  
1002 materials due to  $\pi$ - $\pi$  interactions between layers, which hinders the effective diffusion of  
1003 charges to the active center. In contrast, single-layer or oligomeric CTFs nanosheets have the  
1004 advantage of short migration paths for photogenerated electrons and tunable optoelectronic  
1005 properties. Therefore, the preparation of single-layer or oligomeric CTFs by exfoliation or

1006 interfacial synthesis is considered as an approach to enhance the photocatalytic performance of  
1007 CTFs.

1008       Semiconductor doping is a conventional method used to improve the photocatalytic  
1009 performance of inorganic semiconductor materials. Similarly, doping heteroatoms into the  
1010 CTFs framework can significantly alter its band structure, broaden the light absorption range,  
1011 and enhance carrier mobility. Thus, doping is also a viable approach to enhance the  
1012 photocatalytic performance of CTFs. Moreover, constructing heterostructures can effectively  
1013 promote the separation and migration of photogenerated carriers in CTFs. By utilizing  
1014 electrostatic adsorption, covalent bonding, and  $\pi$ - $\pi$  interactions, CTFs can form heterostructures  
1015 with other semiconductors such as inorganic semiconductor materials, MOFs, and COFs,  
1016 leading to type-II and Z-scheme heterostructures. This enables efficient transfer of  
1017 photogenerated carriers on the contact surface between them, effectively separating electron-  
1018 hole pairs. Additionally, the composites of single atoms and CTFs provide abundant active sites  
1019 for reactions and enhance the conductivity of catalysts, improving the mobility of  
1020 photogenerated electrons.

1021       Although the photocatalytic performance of CTFs has shown notable advancements  
1022 through the aforementioned research and theoretical studies, it is essential to acknowledge that  
1023 there is still room for improvement. The structure-activity relationship of CTFs also requires  
1024 further detailed investigation.

1025       We believe that investigating the following aspects of CTFs will be crucial for future  
1026 applications:

1027       (1) Development of green and scalable synthesis methods: The excellent stability and

1028 nitrogen-rich structure of CTFs not only make them promising for photocatalytic applications  
1029 but also popular in electrocatalysis, industrial catalysis, and other fields.<sup>143, 220-222</sup> There is an  
1030 urgent need to develop a more green, safe, and cost-effective process for large-scale synthesis  
1031 of high-quality CTFs to meet the demands of various industries.

1032 (2) Design of novel structure CTFs and CTFs-organic semiconductor heterojunction: The  
1033 strategies summarized above to improve the photocatalytic performance of CTFs aim to  
1034 broaden the visible light absorption range of CTFs, improve the separation efficiency of  
1035 photogenerated carriers, shorten the migration paths of photogenerated electrons and holes, and  
1036 reduce crystal defects of CTFs. For that purpose, by combining the advantages of various  
1037 strategies, CTFs with high visible light absorption efficiency, high crystallinity, single-layer or  
1038 oligolayer D-A structure can be designed and synthesized. Based on the easy modification of  
1039 CTFs with other organic semiconductor materials, the CTFs-organic semiconductor  
1040 heterojunction constructed through electrostatic adsorption or covalent bonding is easy to  
1041 regulate the band structure and promote the separation and migration of photogenerated carriers.

1042 (3) Mechanistic studies of CTFs in photocatalytic reactions: In-depth investigations are  
1043 necessary to fully understand the mechanisms of CTFs in photocatalytic reactions, especially  
1044 the impact of D-A structures on their performance. Currently, the understanding of the effect  
1045 of D-A structures is largely based on theoretical calculations, and there is a lack of relevant  
1046 experimental characterization. Advanced characterization techniques such as steady-state  
1047 fluorescence emission<sup>100</sup> and time-resolved electron paramagnetic response (TREPR)  
1048 spectroscopy<sup>223</sup> can provide valuable experimental evidence for studying the photogenerated  
1049 electron-hole separation and transfer states during photocatalytic reactions. Such studies would

1050 contribute to a comprehensive understanding of the role of D-A structures in enhancing the  
1051 photocatalytic performance of CTFs.

1052 (4) Photocatalytic CO<sub>2</sub>RR application: CTFs show advantages in adsorbing CO<sub>2</sub> due to  
1053 their N-rich characteristics. However, the research on photocatalytic CO<sub>2</sub>RR is still in its initial  
1054 stages, and in most cases, the CO<sub>2</sub> reduction product is CO. Developing efficient photocatalysts  
1055 for the photocatalytic CO<sub>2</sub>RR to produce valuable organic compounds holds great promise and  
1056 presents an attractive avenue for further research.

1057 (5) Exploration of 3D CTFs: Most current CTF research focuses on 2D structures and less  
1058 work has been done on 3D CTFs.<sup>224</sup> The novel structure of 3D CTFs may offer unexpected  
1059 optoelectronic properties, breaking the barriers of 2D materials.

1060 (6) Utilizing intelligent computing tools: The design of new CTFs for photocatalytic  
1061 applications is often based on existing literature and the experiences of researchers, which may  
1062 not always lead to optimal photocatalytic properties. To address this challenge, the utilization  
1063 of machine learning intelligent computing tools to pre-design high-performance  
1064 photocatalysts,<sup>100, 225</sup> combined with high-throughput technology<sup>226</sup> for rapid prediction of the  
1065 catalytic performance of CTFs, can significantly improve the efficiency of developing new and  
1066 advanced catalysts. By leveraging these advanced techniques, researchers can swiftly identify  
1067 promising CTF candidates with enhanced photocatalytic properties and expedite the discovery  
1068 of high-performance photocatalysts for various applications.

1069 In summary, although still in its early stages, the exciting research on using CTF-based  
1070 materials for photocatalytic applications is already laying the groundwork for effective  
1071 modification strategies and design rules to enhance their photocatalytic performance. With this

1072 strong and encouraging foundation, future efforts hold the promise of having a significant  
1073 impact on solar fuel and chemical production.

1074

#### 1075 **Author contributions**

1076 All the authors contributed to the paper. Yubing Liu: writing - original draft, visualization, and  
1077 funding acquisition. Hao Wu: writing - original draft and visualization. Qian Wang: supervision,  
1078 writing - review & editing, and funding acquisition.

1079

#### 1080 **Conflicts of interest**

1081 There are no conflicts to declare.

1082

#### 1083 **Acknowledgements**

1084 This work was supported by the JSPS Leading Initiative for Excellent Young Researchers  
1085 program (to Q.W.), the JST Fusion Oriented REsearch for disruptive Science and Technology  
1086 program (to Q.W.) and National Natural Science Foundation of China (no. 22002058, to Y. L.).

1087

#### 1088 **Notes and references**

1089 1. A. P. Côté, A. I. Benin, N. W. Ockwig, M. Keeffe, A. J. Matzger and O. M. Yaghi, *Science*,  
1090 2005, **310**, 1166.

1091 2. H. Wang, Y. Yang, X. Yuan, W. Liang Teo, Y. Wu, L. Tang and Y. Zhao, *Mater. Today*, 2022,  
1092 **53**, 106-133.

1093 3. H. Wang, H. Wang, Z. Wang, L. Tang, G. Zeng, P. Xu, M. Chen, T. Xiong, C. Zhou, X. Li, D.  
1094 Huang, Y. Zhu, Z. Wang and J. Tang, *Chem. Soc. Rev.*, 2020, **49**, 4135-4165.

1095 4. G. B. Wang, S. Li, C. X. Yan, F. C. Zhu, Q. Q. Lin, K. H. Xie, Y. Geng and Y. B. Dong, *J.*  
1096 *Mater. Chem. A*, 2020, **8**, 6957-6983.

- 1097 5. K. Kamiya, *Chem. Sci.*, 2020, **11**, 8339-8349.
- 1098 6. G. Zhang, X. Li, Q. Liao, Y. Liu, K. Xi, W. Huang and X. Jia, *Nat. Commun.*, 2018, **9**, 2785.
- 1099 7. R. Liu, K. T. Tan, Y. Gong, Y. Chen, Z. Li, S. Xie, T. He, Z. Lu, H. Yang and D. Jiang, *Chem. Soc. Rev.*, 2021, **50**, 120-242.
- 1101 8. C. Qian, W. Zhou, J. Qiao, D. Wang, X. Li, W. L. Teo, X. Shi, H. Wu, J. Di, H. Wang, G. Liu, L. Gu, J. Liu, L. Feng, Y. Liu, S. Y. Quek, K. P. Loh and Y. Zhao, *J. Am. Chem. Soc.*, 2020, **142**, 18138-18149.
- 1104 9. D. Zhu, G. Xu, M. Barnes, Y. Li, C. P. Tseng, Z. Zhang, J. J. Zhang, Y. Zhu, S. Khalil, M. M. Rahman, R. Verduzco and P. M. Ajayan, *Adv. Funct. Mater.*, 2021, **31**, 2100505.
- 1106 10. J. Wang and S. Zhuang, *Coord. Chem. Rev.*, 2019, **400**, 213046.
- 1107 11. Y. Mou, X. Wu, C. Qin, J. Chen, Y. Zhao, L. Jiang, C. Zhang, X. Yuan, E. Huixiang Ang and H. Wang, *Angew. Chem. Int. Ed.*, 2023, e202309480.
- 1109 12. C. Krishnaraj, H. S. Jena, K. Leus and P. Van Der Voort, *Green Chem.*, 2020, **22**, 1038-1071.
- 1110 13. T. Sun, C. Wang and Y. Xu, *Chem. Res. Chinese. U.*, 2020, **36**, 640-647.
- 1111 14. R. Sun and B. Tan, *Chem. Res. Chinese. U.*, 2022, **38**, 310-324.
- 1112 15. Y. Zhang and S. Jin, *Polymers*, 2019, **11**, 31.
- 1113 16. Z. F. Qian, Z. J. Wang and K. A. I. Zhang, *Chem. Mater.*, 2021, **33**, 1909-1926.
- 1114 17. H. Wang, L. Guan, J. Liu, T. Lei, Y. Xue, Z. Qu, S. Jin, H. Ma and Z. Guo, *J. Mater. Chem. A*, 2022, **10**, 16328-16336.
- 1116 18. L. Guo, X. Wang, Z. Zhan, Y. Zhao, L. Chen, T. Liu, B. Tan and S. Jin, *Chem. Mater.*, 2021, **33**, 1994-2003.
- 1118 19. Z. Qian, Z. J. Wang and K. A. I. Zhang, *Chem. Mater.*, 2021, **33**, 1909-1926.

- 1119 20. F. Niu, L. Tao, Y. Deng, H. Gao, J. Liu and W. Song, *New J. Chem.*, 2014, **38**, 5695-5699.
- 1120 21. C. Yang, W. Huang, L. C. da Silva, K. A. I. Zhang and X. Wang, *Chem-Eur. J.*, 2018, **24**,  
1121 17454-17458.
- 1122 22. Y. Cong, X. Chen, W. Wang and S.W. Lv, *New J. Chem.*, 2021, **45**, 21278-21284.
- 1123 23. H. Lin, C. Chen, T. Zhou and J. Zhang, *Sol. RRL*, 2020, **5**, 2000458.
- 1124 24. M. Liu, L. Guo, S. Jin and B. Tan, *J. Mater. Chem. A*, 2019, **7**, 5153-5172.
- 1125 25. S. Zhang, G. Cheng, L. Guo, N. Wang, B. Tan and S. Jin, *Angew. Chem., Int. Ed.*, 2020, **59**,  
1126 6007-6014.
- 1127 26. S. Tao and D. Jiang, *CCS Chem.*, 2021, **3**, 2003-2024.
- 1128 27. Q. Wang and K. Domen, *Chem. Rev.*, 2020, **120**, 919-985.
- 1129 28. J. Ozdemir, I. Mosleh, M. Abolhassani, L. F. Greenlee, R. R. Beitle and M. H. Beyzavi, *Front.*  
1130 *Energy Res.*, 2019, **7**.
- 1131 29. A. Fujishima and K. Honda, *Nature*, 1972, **238**, 37-38.
- 1132 30. H. W. Li, Z. Guan, Y. Cheng, T. Lui, Q. Yang, C. S. Lee, S. Chen and S. W. Tsang, *Adv.*  
1133 *Electron. Mater.*, 2016, **2**, 1600200.
- 1134 31. S. Zhu and D. Wang, *Adv. Energy Mater.*, 2017, **7**, 1700841.
- 1135 32. X. Chang, T. Wang and J. Gong, *Energy Environ. Sci.*, 2016, **9**, 2177-2196.
- 1136 33. E. Gong, S. Ali, C. B. Hiragond, H. S. Kim, N. S. Powar, D. Kim, H. Kim and S. I. In, *Energy*  
1137 *Environ. Sci.*, 2022, **15**, 880-937.
- 1138 34. V. S. Vyas, F. Haase, L. Stegbauer, G. Savasci, F. Podjaski, C. Ochsenfeld and B. V. Lotsch,  
1139 *Nat. Commun.*, 2015, **6**, 8508.
- 1140 35. R. Sun and B. Tan, *Chem-Eur. J.*, 2023, **29**, e202203077.



- 1141 36. S. Zhang, F. Zhao, G. Yasin, Y. Dong, J. Zhao, Y. Guo, P. Tsiakaras and J. Zhao, *J. Colloid*  
1142 *Interface Sci.*, 2023, **637**, 41-54.
- 1143 37. G. Tuci, M. Pugliesi, A. Rossin, C. Pham-Huu, E. Berretti and G. Giambastiani, *Chemistryselect*,  
1144 2022, **7**, e20220356.
- 1145 38. P. Puthiaraj and W. S. Ahn, *J. Energy Chem.*, 2017, **26**, 965-971.
- 1146 39. R. Luo, W. Xu, M. Chen, X. Liu, Y. Fang and H. Ji, *ChemSusChem*, 2020, **13**, 6509-6522.
- 1147 40. Y. Zou, S. Abednatanzi, P. Gohari Derakhshandeh, S. Mazzanti, C. M. Schüßlbauer, D. Cruz,  
1148 P. Van Der Voort, J. W. Shi, M. Antonietti, D. M. Guldi and A. Savateev, *Nat. Commun.*, 2022,  
1149 **13**, 2171.
- 1150 41. Y. Sun, W. Li, Z. Wang, J. Shi and Z. Jiang, *Curr. Opin. Biotechnol.*, 2022, **73**, 67-73.
- 1151 42. M. R. Hoffmann, S. T. Martin, W. Choi and D. W. Bahnemann, *Chem. Rev.*, 1995, **95**, 69-96.
- 1152 43. X. An, T. Li, B. Wen, J. Tang, Z. Hu, L. M. Liu, J. Qu, C. P. Huang and H. Liu, *Adv. Energy*  
1153 *Mater.*, 2016, **6**, 1502268.
- 1154 44. R. Abe, *J Photoch Photobio C.*, 2010, **11**, 179-209.
- 1155 45. Y. Sasaki, A. Iwase, H. Kato and A. Kudo, *J. Catal.*, 2008, **259**, 133-137.
- 1156 46. W. Kurashige, Y. Mori, S. Ozaki, M. Kawachi, S. Hossain, T. Kawawaki, C. J. Shearer, A.  
1157 Iwase, G. F. Metha, S. Yamazoe, A. Kudo and Y. Negishi, *Angew. Chem. Int. Ed.*, 2020, **59**,  
1158 7076-7082.
- 1159 47. F. Haase, T. Banerjee, G. Savasci, C. Ochsenfeld and B. V. Lotsch, *Faraday Discuss.*, 2017,  
1160 **201**, 247-264.
- 1161 48. L. De Bruecker, J. Everaert, P. Van Der Voort, C. V. Stevens, M. Waroquier and V. Van  
1162 Speybroeck, *ChemPhysChem*, 2020, **21**, 2489-2505.

- 1163 49. H. Liu, C. Li, H. Li, Y. Ren, J. Chen, J. Tang and Q. Yang, *ACS Appl. Mater. Interfaces*, 2020,  
1164 **12**, 20354-20365.
- 1165 50. A. López-Magano, N. Salaverri, L. Marzo, R. Mas-Ballesté and J. Alemán, *Appl. Catal., B*,  
1166 2022, **317**, 121791.
- 1167 51. M. Alves Fávaro, D. Ditz, J. Yang, S. Bergwinkl, A. C. Ghosh, M. Stammer, C. Lorentz, J.  
1168 Roeser, E. A. Quadrelli, A. Thomas, R. Palkovits, J. Canivet and F. M. Wissler, *ACS Appl. Mater.*  
1169 *Interfaces*, 2022, **14**, 14182-14192.
- 1170 52. Y. Yang, X. Chu, H.Y. Zhang, R. Zhang, Y. H. Liu, F. M. Zhang, M. Lu, Z. D. Yang and Y. Q.  
1171 Lan, *Nat. Commun.*, 2023, **14**, 593.
- 1172 53. Z. Zhao, X. Chen, B. Li, S. Zhao, L. Niu, Z. Zhang and Y. Chen, *Adv. Sci.*, 2022, **9**, 2203832.
- 1173 54. V. S. Vyas, F. Haase, L. Stegbauer, G. Savasci, F. Podjaski, C. Ochsenfeld and B. V. Lotsch,  
1174 *Nat. Commun.*, 2015, **6**, 8508.
- 1175 55. G. Cheng, K. Wang, S. Wang, L. Guo, Z. Wang, J. Jiang, B. Tan and S. Jin, *Sci. China Mater.*,  
1176 2021, **64**, 149-157.
- 1177 56. H. Wang, L. Guan, J. Liu, T. Lei, Y. Xue, Z. Qu, S. Jin, H. Ma and Z. Guo, *J. Mater. Chem. A*,  
1178 2022, **10**, 16328-16336.
- 1179 57. Q. Sheng, X. Zhong, Q. Shang, Y. Dong, J. Zhao, Y. Du and Y. Xie, *Front. Chem.*, 2022, **10**,  
1180 854018.
- 1181 58. C. Wu, Z. Teng, C. Yang, F. Chen, H. B. Yang, L. Wang, H. Xu, B. Liu, G. Zheng and Q. Han,  
1182 *Adv. Mater.*, 2022, **34**, 2110266.
- 1183 59. X. Yu, B. Viengkeo, Q. He, X. Zhao, Q. Huang, P. Li, W. Huang and Y. Li, *Adv. Sustainable*  
1184 *Syst.*, 2021, **5**, 2100184.

- 1185 60. W. Huang, N. Huber, S. Jiang, K. Landfester and K. A. I. Zhang, *Angew. Chem. Int. Ed.*, 2020,  
1186 **59**, 18368-18373.
- 1187 61. X. Wang, L. Chen, S. Y. Chong, M. A. Little, Y. Wu, W.-H. Zhu, R. Clowes, Y. Yan, M. A.  
1188 Zwijnenburg, R. S. Sprick and A. I. Cooper, *Nat. Chem.*, 2018, **10**, 1180-1189.
- 1189 62. W. Zhang, Z. Deng, J. Deng, C.T. Au, Y. Liao, H. Yang and Q. Liu, *J. Mater. Chem. A*, 2022,  
1190 **10**, 22419-22427.
- 1191 63. M. Liu, K. Yang, Z. Li, E. Fan, H. Fu, L. Zhang, Y. Zhang and Z. Zheng, *Chem. Commun.*,  
1192 2022, **58**, 92-95.
- 1193 64. M. Xiao, R. L. Carey, H. Chen, X. Jiao, V. Lemaire, S. Schott, M. Nikolka, C. Jellett, A.  
1194 Sadhanala, S. Rogers, S. P. Senanayak, A. Onwubiko, S. Han, Z. Zhang, M. Abdi-Jalebi, Y.  
1195 Zhang, T. H. Thomas, N. Mahmoudi, L. Lai, E. Selezneva, X. Ren, M. Nguyen, Q. Wang, I.  
1196 Jacobs, W. Yue, C. R. McNeill, G. Liu, D. Beljonne, I. McCulloch and H. Sirringhaus, *Sci.*  
1197 *Adv.*, 2021, **7**, eabe5280.
- 1198 65. M. Seri and A. Marrocchi, *J. Mater. Chem. C*, 2021, **9**, 16164-16186.
- 1199 66. A. Acharjya, L. Longworth-Dunbar, J. Roeser, P. Pachfule and A. Thomas, *J. Am. Chem. Soc.*,  
1200 2020, **142**, 14033-14038.
- 1201 67. Z. Wang, Y. Yang, Z. Zhao, P. Zhang, Y. Zhang, J. Liu, S. Ma, P. Cheng, Y. Chen and Z. Zhang,  
1202 *Nat. Commun.*, 2021, **12**, 1982.
- 1203 68. S. Wei, F. Zhang, W. Zhang, P. Qiang, K. Yu, X. Fu, D. Wu, S. Bi and F. Zhang, *J. Am. Chem.*  
1204 *Soc.*, 2019, **141**, 14272-14279.
- 1205 69. Y. Yang, H. Niu, L. Xu, H. Zhang and Y. Cai, *Appl. Catal., B*, 2020, **269**, 118799.
- 1206 70. H. Hao, F. Zhang, X. Dong and X. Lang, *Appl. Catal., B*, 2021, **299**, 120691.

- 1207 71. F. Zhang, H. Hao, X. Dong, X. Li and X. Lang, *Appl. Catal., B*, 2022, **305**, 121027.
- 1208 72. L. Chen, L. Wang, Y. Wan, Y. Zhang, Z. Qi, X. Wu and H. Xu, *Adv. Mater.*, 2020, **32**, 1904433.
- 1209 73. L. Zhai, Z. Xie, C.X. Cui, X. Yang, Q. Xu, X. Ke, M. Liu, L. B. Qu, X. Chen and L. Mi, *Chem. Mater.*, 2022, **34**, 5232-5240.
- 1210
- 1211 74. X. Lan, J. Wang, Q. Li, A. Wang, Y. Zhang, X. Yang and G. Bai, *ChemSusChem*, 2022, **15**,  
1212 e202102455.
- 1213 75. X. Lan, X. Liu, Y. Zhang, Q. Li, J. Wang, Q. Zhang and G. Bai, *ACS Catal.*, 2021, **11**, 7429-  
1214 7441.
- 1215 76. T. Lei, Y. Mi, Z. Wei, S. Li and S. Pang, *Dalton Trans.*, 2023, **52**, 1761-1767.
- 1216 77. J. Barber, *Chem. Soc. Rev.*, 2009, **38**, 185-196.
- 1217 78. S. M. Sartor, Y. M. Lattke, B. G. McCarthy, G. M. Miyake and N. H. Damrauer, *J. Phys. Chem. A*, 2019, **123**, 4727-4736.
- 1218
- 1219 79. Q. Zhang, J. Chen, H. Che, P. Wang, B. Liu and Y. Ao, *ACS Mater. Lett.*, 2022, **4**, 2166-2186.
- 1220 80. L. Guo, Y. Niu, S. Razzaque, B. Tan and S. Jin, *ACS Catal.*, 2019, **9**, 9438-9445.
- 1221 81. G. J. Hedley, A. Ruseckas and I. D. W. Samuel, *Chem. Rev.*, 2017, **117**, 796-837.
- 1222 82. Y. Xu, P. Xu, D. Hu and Y. Ma, *Chem. Soc. Rev.*, 2021, **50**, 1030-1069.
- 1223 83. L. Wu, C. Huang, B. P. Emery, A. C. Sedgwick, S. D. Bull, X. P. He, H. Tian, J. Yoon, J. L. Sessler and T. D. James, *Chem. Soc. Rev.*, 2020, **49**, 5110-5139.
- 1224
- 1225 84. Z. A. Lan, X. Chi, M. Wu, X. Zhang, X. Chen, G. Zhang and X. Wang, *Small*, 2022, **18**, 2200129.
- 1226 85. Y. Hu, W. Huang, H. Wang, Q. He, Y. Zhou, P. Yang, Y. Li and Y. Li, *Angew. Chem. Int. Ed.*,  
1227 2020, **59**, 14378-14382.
- 1228 86. W. Y. Geng, X. X. Lu, H. Zhang, Y. H. Luo, Z. X. Wang, S. F. Guo, Z. Y. Zhou and D. E.

- 1229 Zhang, *Sep. Purif. Technol.*, 2022, **290**, 120829.
- 1230 87. W. Huang, J. Byun, I. Rörich, C. Ramanan, P. W. M. Blom, H. Lu, D. Wang, L. Caire da Silva,  
1231 R. Li, L. Wang, K. Landfester and K. A. I. Zhang, *Angew. Chem. Int. Ed.*, 2018, **57**, 8316-8320.
- 1232 88. C. Wang, H. Zhang, W. Luo, T. Sun and Y. Xu, *Angew. Chem. Int. Ed.*, 2021, **60**, 25381-25390.
- 1233 89. G. B. Wang, F. C. Zhu, Q. Q. Lin, J. L. Kan, K. H. Xie, S. Li, Y. Geng and Y. B. Dong, *Chem.*  
1234 *Commun.*, 2021, **57**, 4464-4467.
- 1235 90. B. Fuerte-Diez, A. Valverde-Gonzalez, M. Pintado-Sierra, U. Diaz, F. Sanchez, E. M. Maya  
1236 and M. Iglesias, *Sol. RRL*, 2022, **6**, 2100848.
- 1237 91. L. Guo, Y. Niu, H. Xu, Q. Li, S. Razzaque, Q. Huang, S. Jin and B. Tan, *J. Mater. Chem. A*,  
1238 2018, **6**, 19775-19781.
- 1239 92. H. Zhong, Z. Hong, C. Yang, L. Li, Y. Xu, X. Wang and R. Wang, *ChemSusChem*, 2019, **12**,  
1240 4493-4499.
- 1241 93. B. W. Cai, L. Cao, R. J. Zhang, N. Z. Xu, J. Tang, K. Q. Wang, Q. Li, B. L. Xu, Y. B. Liu and  
1242 Y. N. Fan, *ACS Appl. Energy Mater.*, 2023, **6**, 930-938.
- 1243 94. B. Wu, Y. Liu, Y. X. Zhang, L. Fan, Q. Y. Li, Z. Y. Yu, X. S. Zhao, Y. C. Zheng and X. J.  
1244 Wang, *J. Mater. Chem. A*, 2022, **10**, 12489-12496.
- 1245 95. W. Huang, Q. He, Y. Hu and Y. Li, *Angew. Chem. Int. Ed.*, 2019, **58**, 8676-8680.
- 1246 96. C. Ayed, W. Huang and K. A. I. Zhang, *Front. Chem. Sci. Eng.*, 2020, **14**, 397-404.
- 1247 97. C. Ayed, J. Yin, K. Landfester and K. Zhang, *Angew. Chem. Int. Ed.*, 2023, **62**, e202216159.
- 1248 98. W. Huang, B. C. Ma, H. Lu, R. Li, L. Wang, K. Landfester and K. A. I. Zhang, *ACS Catal.*,  
1249 2017, **7**, 5438-5442.
- 1250 99. C. Ayed, W. Huang, G. Kizilsavas, K. Landfester and K. A. I. Zhang, *ChemPhotoChem*, 2020,

- 1251 4, 571-576.
- 1252 100. Y. Qian, Y. Han, X. Zhang, G. Yang, G. Zhang and H. L. Jiang, *Nat. Commun.*, 2023, **14**, 3083.
- 1253 101. J. Yu, S. Chang, X. Xu, X. He and C. Zhang, *J. Mater. Chem. C*, 2020, **8**, 8887-8895.
- 1254 102. H. Wang, C. Yang, F. Chen, G. Zheng and Q. Han, *Angew. Chem. Int. Ed.*, 2022, **61**,
- 1255 e202202328.
- 1256 103. H. Ye, N. Gong, Y. Cao, X. Fan, X. Song, H. Li, C. Wang, Y. Mei and Y. Zhu, *Chem. Mater.*,
- 1257 2022, **34**, 1481-1490.
- 1258 104. J. Yang, A. Acharjya, M. Y. Ye, J. Rabeah, S. Li, Z. Kochovski, S. Youk, J. Roeser, J.
- 1259 Grüneberg, M. Schwarze, T. Wang, Y. Lu, R. van de Krol, M. Oschatz, R. Schomäcker, P.
- 1260 Saalfrank, A. Thomas and C. Penschke, *Angew. Chem. Int. Ed.*, 2021, **60**, 19797-19803.
- 1261 105. B. Cai, L. Cao, R. Zhang, N. Xu, J. Tang, K. Wang, Q. Li, B. Xu, Y. Liu and Y. Fan, *ACS Appl.*
- 1262 *Energy Mater.*, 2023, **6**, 930-938.
- 1263 106. F. Yang, J. Qu, Y. Zheng, Y. Cai, X. Yang, C. M. Li and J. Hu, *Nanoscale*, 2022, **14**, 15217-
- 1264 15241.
- 1265 107. B. Mishra, A. Alam, B. Kumbhakar, D. D. Díaz and P. Pachfule, *Cryst. Growth Des.*, 2023, **23**,
- 1266 4701-4719.
- 1267 108. X. Wang, S. Zhang, X. Li, Z. Zhan, B. Tan, X. Lang and S. Jin, *J. Mater. Chem. A*, 2021, **9**,
- 1268 16405-16410.
- 1269 109. S. Ren, M. J. Bojdys, R. Dawson, A. Laybourn, Y. Z. Khimiyak, D. J. Adams and A. I. Cooper,
- 1270 *Adv. Mater.*, 2012, **24**, 2357-2361.
- 1271 110. M. Liu, K. Jiang, X. Ding, S. Wang, C. Zhang, J. Liu, Z. Zhan, G. Cheng, B. Li, H. Chen, S. Jin
- 1272 and B. Tan, *Adv. Mater.*, 2019, **31**, 1807865.

- 1273 111. S. Kuecken, A. Acharjya, L. Zhi, M. Schwarze, R. Schomaecker and A. Thomas, *Chem.*  
1274 *Commun.*, 2017, **53**, 5854-5857.
- 1275 112. P. Kuhn, M. Antonietti and A. Thomas, *Angew. Chem. Int. Ed.*, 2008, **47**, 3450-3453.
- 1276 113. P. Kuhn, A. Forget, D. Su, A. Thomas and M. Antonietti, *J. Am. Chem. Soc.*, 2008, **130**, 13333-  
1277 13337.
- 1278 114. S. Hug, M. E. Tauchert, S. Li, U. E. Pachmayr and B. V. Lotsch, *J. Mater. Chem.*, 2012, **22**,  
1279 13956-13964.
- 1280 115. A. Bhunia, I. Boldog, A. Moeller and C. Janiak, *J. Mater. Chem. A*, 2013, **1**, 14990-14999.
- 1281 116. A. Bhunia, D. Esquivel, S. Dey, R. Fernandez-Teran, Y. Goto, S. Inagaki, P. Van der Voort and  
1282 C. Janiak, *J. Mater. Chem. A*, 2016, **4**, 13450-13457.
- 1283 117. X. Zhu, C. Tian, S. M. Mahurin, S. H. Chai, C. Wang, S. Brown, G. M. Veith, H. Luo, H. Liu  
1284 and S. Dai, *J. Am. Chem. Soc.*, 2012, **134**, 10478-10484.
- 1285 118. Z. Yang, T. Liu, S. Wang, H. Chen, X. Suo, T. Wang, B. P. Thapaliya, D.-e. Jiang, I. Popovs  
1286 and S. Dai, *Chem. Mater.*, 2021, **33**, 3386-3393.
- 1287 119. T. Sun, Y. Liang, W. Luo, L. Zhang, X. Cao and Y. Xu, *Angew. Chem. Int. Ed.*, 2022, **61**,  
1288 e202203327.
- 1289 120. K. Wang, L. Yang, X. Wang, L. Guo, Gg. Cheng, C. Zhang, S. Jin, B. Tan and A. Cooper,  
1290 *Angew. Chem. Int. Ed.*, 2017, **56**, 14149-14153.
- 1291 121. L. Guan, G. Cheng, B. Tan and S. Jin, *Chem. Commun.*, 2021, **57**, 5147-5150.
- 1292 122. X. Hu, Z. Zhan, J. Zhang, I. Hussain and B. Tan, *Nat. Commun.*, 2021, **12**, 6596.
- 1293 123. S. Y. Yu, J. Mahmood, H. J. Noh, J. M. Seo, S. M. Jung, S. H. Shin, Y. K. Im, I. Y. Jeon and J.  
1294 B. Baek, *Angew. Chem. Int. Ed.*, 2018, **57**, 8438-8442.

- 1295 124. P. Katekomol, J. Roeser, M. Bojdys, J. Weber and A. Thomas, *Chem. Mater.*, 2013, **25**, 1542-  
1296 1548.
- 1297 125. M. J. Bojdys, J. Jeromenok, A. Thomas and M. Antonietti, *Adv. Mater.*, 2010, **22**, 2202-2205.
- 1298 126. J. Maschita, T. Banerjee, G. Savasci, F. Haase, C. Ochsenfeld and B. V. Lotsch, *Angew. Chem.*  
1299 *Int. Ed.*, 2020, **59**, 15750-15758.
- 1300 127. Z. A. Lan, M. Wu, Z. Fang, Y. Zhang, X. Chen, G. Zhang and X. Wang, *Angew. Chem. Int. Ed.*,  
1301 2022, **61**, e202201482.
- 1302 128. J. Bi, W. Fang, L. Li, J. Wang, S. Liang, Y. He, M. Liu and L. Wu, *Macromol. Rapid Commun.*,  
1303 2015, **36**, 1799-1805.
- 1304 129. J. Xie, S. A. Shevlin, Q. Ruan, S. J. A. Moniz, Y. Liu, X. Liu, Y. Li, C. C. Lau, Z. X. Guo and  
1305 J. Tang, *Energy Environ. Sci.*, 2018, **11**, 1617-1624.
- 1306 130. T. Sun, Y. Liang and Y. Xu, *Angew. Chem., Int. Ed.*, 2022, **61**, e202113926.
- 1307 131. M. Liu, Q. Huang, S. Wang, Z. Li, B. Li, S. Jin and B. Tan, *Angew. Chem. Int. Ed.*, 2018, **57**,  
1308 11968-11972.
- 1309 132. W. Cen, T. Xiong, C. Tang, S. Yuan and F. Dong, *Ind. Eng. Chem. Res.*, 2014, **53**, 15002-  
1310 15011.
- 1311 133. T. Gyulavári, G. Veréb, Z. Pap, A. Dombi and K. Hernádi, *Catal. Today*, 2018, **313**, 231-238.
- 1312 134. K. Schwinghammer, S. Hug, M. B. Mesch, J. Senker and B. V. Lotsch, *Energy Environ. Sci.*,  
1313 2015, **8**, 3345-3353.
- 1314 135. D. Kong, X. Han, J. Xie, Q. Ruan, C. D. Windle, S. Gadipelli, K. Shen, Z. Bai, Z. Guo and J.  
1315 Tang, *ACS Catal.*, 2019, **9**, 7697-7707.
- 1316 136. N. Wang, G. Cheng, L. Guo, B. Tan and S. Jin, *Adv. Funct. Mater.*, 2019, **29**, 1904781.



- 1317 137. W. Huang, Z. J. Wang, B. C. Ma, S. Ghasimi, D. Gehrig, F. Laquai, K. Landfester and K. A. I.  
1318 Zhang, *J. Mater. Chem. A*, 2016, **4**, 7555-7559.
- 1319 138. H. Wang, Z. Zeng, P. Xu, L. Li, G. Zeng, R. Xiao, Z. Tang, D. Huang, L. Tang, C. Lai, D. Jiang,  
1320 Y. Liu, H. Yi, L. Qin, S. Ye, X. Ren and W. Tang, *Chem. Soc. Rev.*, 2019, **48**, 488-516.
- 1321 139. Y. Tao, W. Ji, X. Ding and B. H. Han, *J. Mater. Chem. A*, 2021, **9**, 7336-7365.
- 1322 140. L. Li, Y. Zhu, N. Gong, W. Zhang, W. Peng, Y. Li, F. Zhang and X. Fan, *Int. J. Hydrogen  
1323 Energy*, 2020, **45**, 2689-2698.
- 1324 141. J. Liu, M. Liu, X. Wang, K. Wang, S. Jin and B. Tan, *Adv. Mater. Interfaces*, 2021, **8**, 2100374.
- 1325 142. Y. Z. Zhu, M. Qiao, W. C. Peng, Y. Li, G. L. Zhang, F. B. Zhang, Y. F. Li and X. B. Fan, *J.  
1326 Mater. Chem. A*, 2017, **5**, 9272-9278.
- 1327 143. Z. Lei, X. Chen, W. Sun, Y. Zhang and Y. Wang, *Adv. Energy Mater.*, 2019, **9**, 1801010.
- 1328 144. H. Zhang, W. Sun, X. Chen and Y. Wang, *ACS Nano*, 2019, **13**, 14252-14261.
- 1329 145. J. Liu, P. Lyu, Y. Zhang, P. Nachtigall and Y. Xu, *Adv. Mater.*, 2018, **30**, 1705401.
- 1330 146. Y. P. Tang, H. Wang and T. S. Chung, *ChemSusChem*, 2015, **8**, 138-147.
- 1331 147. J. Liu, W. Zan, K. Li, Y. Yang, F. Bu and Y. Xu, *J. Am. Chem. Soc.*, 2017, **139**, 11666-11669.
- 1332 148. G. Li, W. Wang, Q. Fang and F. Liu, *J. Membr. Sci.*, 2020, **595**, 117525.
- 1333 149. C. Yin, Z. Zhang, J. Zhou and Y. Wang, *ACS Appl. Mater. Interfaces*, 2020, **12**, 18944-18951.
- 1334 150. K. Wang, H. Yang, Z. Liao, S. Li, M. Hamsch, G. Fu, S. C. B. Mannsfeld, Q. Sun and T.  
1335 Zhang, *J. Am. Chem. Soc.*, 2023, **145**, 5203-5210.
- 1336 151. W. Zhao, J. Ding, Y. Zou, C.-a. Di and D. Zhu, *Chem. Soc. Rev.*, 2020, **49**, 7210-7228.
- 1337 152. B. Lüssem, M. Riede and K. Leo, *Phys. Status Solidi A*, 2013, **210**, 9-43.
- 1338 153. Z. Cheng, K. Zheng, G. Lin, S. Fang, L. Li, J. Bi, J. Shen and L. Wu, *Nanoscale Adv.*, 2019, **1**,

- 1339 2674-2680.
- 1340 154. S. Li, M. F. Wu, T. Guo, L. L. Zheng, D. Wang, Y. Mu, Q. J. Xing and J. P. Zou, *Appl. Catal.,*  
1341 *B*, 2020, **272**, 118989.
- 1342 155. X. Han, F. Zhao, Q. Shang, J. Zhao, X. Zhong and J. Zhang, *ChemSusChem*, 2022, **15**,  
1343 e202200828.
- 1344 156. Q. Niu, Z. Cheng, Q. S. Chen, G. C. Huang, J. Y. Lin, J. H. Bi and L. Wu, *ACS Sustainable*  
1345 *Chem. Eng.*, 2021, **9**, 1333-1340.
- 1346 157. Z. Cheng, W. Fang, T. Zhao, S. Fang, J. Bi, S. Liang, L. Li, Y. Yu and L. Wu, *ACS Appl. Mater.*  
1347 *Interfaces*, 2018, **10**, 41415-41421.
- 1348 158. L. Li, W. Fang, P. Zhang, J. Bi, Y. He, J. Wang and W. Su, *J. Mater. Chem. A*, 2016, **4**, 12402-  
1349 12406.
- 1350 159. J. Low, J. Yu, M. Jaroniec, S. Wageh and A. A. Al-Ghamdi, *Adv. Mater.*, 2017, **29**, 1601694.
- 1351 160. H. Yang, *Mater. Res. Bull.*, 2021, **142**, 111406.
- 1352 161. M. Lin, H. Chen, Z. Zhang and X. Wang, *Phys. Chem. Chem. Phys.*, 2023, **25**, 4388-4407.
- 1353 162. Q. Pan, T. Chen, L. Ma, G. Wang, W. B. Hu, Z. Zou, K. Wen and H. Yang, *Chem. Mater.*, 2019,  
1354 **31**, 8062-8068.
- 1355 163. J. Zhang, X. Chen, Q. Chen, Y. He, M. Pan, G. Huang and J. Bi, *Nanomaterials*, 2022, **12**, 4111.
- 1356 164. K. Chen, A. Cai and T. T. Li, *ChemSusChem*, 2023, **16**, e202300021.
- 1357 165. D. Wang, X. Li, L. L. Zheng, L. M. Qin, S. Li, P. Ye, Y. Li and J. P. Zou, *Nanoscale*, 2018, **10**,  
1358 19509-19516.
- 1359 166. D. Wang, H. Zeng, X. Xiong, M. F. Wu, M. Xia, M. Xie, J. P. Zou and S. L. Luo, *Sci. Bull.*,  
1360 2020, **65**, 113-122.

- 1361 167. G. Y. Lin, L. Sun, G. C. Huang, Q. S. Chen, S. Q. Fang, J. H. Bi and L. Wu, *Sustain. Energ. Fuels*, 2021, **5**, 732-739.
- 1362
- 1363 168. B. P. Mishra and K. Parida, *J. Mater. Chem. A*, 2021, **9**, 10039-10080.
- 1364 169. G. Li, J. Ye, Y. Shen, Q. Fang and F. Liu, *Chem. Eng. J.*, 2021, **421**, 127784.
- 1365 170. S. Guo, P. Yang, Y. Zhao, X. Yu, Y. Wu, H. Zhang, B. Yu, B. Han, M. W. George and Z. Liu, *ChemSusChem*, 2020, **13**, 6278-6283.
- 1366
- 1367 171. C. Cui, X. Zhao, X. Su, N. Xi, X. Wang, X. Yu, X. L. Zhang, H. Liu and Y. Sang, *Adv. Funct. Mater.*, 2022, **32**, 2208962.
- 1368
- 1369 172. J. He, X. Wang, S. Jin, Z. Q. Liu and M. Zhu, *Chin. J. Catal.*, 2022, **43**, 1306-1315.
- 1370 173. L. W. Zhang, Y. M. Zhang, X. J. Huang, L. M. Tao and Y. P. Bi, *Appl. Catal., B*, 2021, **283**, 119633.
- 1371
- 1372 174. H. Wang, Y. Wu, M. Feng, W. Tu, T. Xiao, T. Xiong, H. Ang, X. Yuan and J. W. Chew, *Water Res.*, 2018, **144**, 215-225.
- 1373
- 1374 175. L. L. Zheng, D. Wang, S. L. Wu, X. H. Jiang, J. Zhang, Q. J. Xing, J. P. Zou and S. L. Luo, *J. Mater. Chem. A*, 2020, **8**, 25425-25430.
- 1375
- 1376 176. N. Z. Xu, Y. B. Liu, W. J. Yang, J. Tang, B. W. Cai, Q. Li, J. W. Sun, K. Q. Wang, B. L. Xu, Q. T. Zhang and Y. N. Fan, *ACS Appl. Energy Mater.*, 2020, **3**, 11939-11946.
- 1377
- 1378 177. Y. Wang, Q. Yang, F. Yi, R. Lu, Y. Chen, C. Liu, X. Li, C. Wang and H. Yan, *ACS Appl. Mater. Interfaces*, 2021, **13**, 29916-29925.
- 1379
- 1380 178. L. H. Shao, A. X. Huang, X. C. Yan, Y. H. Liu, Y. Wang, X. Jin and F. M. Zhang, *J. Colloid Interface Sci.*, 2023, **633**, 233-242.
- 1381
- 1382 179. X. Han, Y. Dong, J. Zhao, S. Ming and Y. Xie, *Int. J. Hydrogen Energy*, 2022, **47**, 18334-

- 1383 18346.
- 1384 180. Z. Xu, Y. Cui, D. J. Young, J. Wang, H. Y. Li, G. Q. Bian and H. X. Li, *J. CO<sub>2</sub> Util.*, 2021, **49**,
- 1385 101561.
- 1386 181. E. Saputra, B. A. Prawiranegara, M. W. Nugraha, N. S. Sambudi, H. Sugesti, A. Awaluddin,
- 1387 Komalasari, P. S. Utama and M. Manawan, *Environ. Sci. Pollut. Res.*, 2023, **30**, 39961-39977.
- 1388 182. Y. Wang, Z. Hu, W. Wang, Y. Li, H. He, L. Deng, Y. Zhang, J. Huang, N. Zhao, G. Yu and Y.
- 1389 N. Liu, *Appl. Catal., B*, 2023, **327**, 122419.
- 1390 183. Y. L. Yan, Q. J. Fang, J. K. Pan, J. Yang, L. I. Zhang, W. Zhang, G. L. Zhuang, X. Zhong, S.
- 1391 W. Deng and J. G. Wang, *Chem. Eng. J.*, 2021, **408**, 127358.
- 1392 184. K. Ren, S. Yue, C. Li, Z. Fang, K. A. M. Gasem, J. Leszczynski, S. Qu, Z. Wang and M. Fan,
- 1393 *J. Mater. Chem. A*, 2022, **10**, 407-429.
- 1394 185. Q. Wang, J. Wang, J. C. Wang, X. Hu, Y. Bai, X. Zhong and Z. Li, *ChemSusChem*, 2021, **14**,
- 1395 1131-1139.
- 1396 186. Y. Zheng, T. Gao, S. Chen, C. T. J. Ferguson, K. A. I. Zhang, F. Fang, Y. Shen, N. A. Khan, L.
- 1397 Wang and L. Ye, *Compos. Commun.*, 2022, **36**, 101390.
- 1398 187. S. Guo, P. Yang, Y. Zhao, X. Yu, Y. Wu, H. Zhang, B. Yu, B. Han, M. W. George and Z. Liu,
- 1399 *ChemSusChem*, 2020, **13**, 6278-6283.
- 1400 188. G. C. Huang, Q. Niu, J. W. Zhang, H. M. Huang, Q. S. Chen, J. H. Bi and L. Wu, *Chem. Eng.*
- 1401 *J.*, 2022, **427**, 131018.
- 1402 189. G. C. Huang, Q. Niu, Y. X. He, J. J. Tian, M. B. Gao, C. Y. Li, N. An, J. H. Bi and J. W. Zhang,
- 1403 *Nano Res.*, 2022, **15**, 8001-8009.
- 1404 190. L. Ran, Z. W. Li, B. Ran, J. Q. Cao, Y. Zhao, T. Shao, Y. R. Song, M. K. H. Leung, L. C. Sun

- 1405 and J. A. Hou, *J. Am. Chem. Soc.*, 2022, **144**, 17097-17109.
- 1406 191. Y. He, X. Chen, C. Huang, L. Li, C. Yang and Y. Yu, *Chin. J. Catal.*, 2021, **42**, 123-130.
- 1407 192. J. Li, P. Liu, Y. Tang, H. Huang, H. Cui, D. Mei and C. Zhong, *ACS Catal.*, 2020, **10**, 2431-
- 1408 2442.
- 1409 193. S. J. Gao, P. Zhang, G. C. Huang, Q. S. Chen, J. H. Bi and L. Wu, *Chemsuschem*, 2021, **14**,
- 1410 3850-3857.
- 1411 194. Z. W. Li, S. Qiu, Y. R. Song, S. Y. Huang, J. F. Gao, L. C. Sun and J. A. Hou, *Sci. Bull.*, 2022,
- 1412 **67**, 1971-1981.
- 1413 195. Z. Xu, Y. Cui, B. Guo, H. Y. Li and H. X. Li, *ChemCatChem*, 2021, **13**, 958-965.
- 1414 196. D. A. Bulushev, F. S. Golub, S. V. Trubina, V. V. Zvereva, L. G. Bulusheva, E. Y. Gerasimov,
- 1415 M. Navlani-Garcia, A. D. Krot and H. S. Jena, *ACS Appl. Nano Mater.*, 2022, **5**, 12887-12896.
- 1416 197. N. F. Xu, Y. X. Diao, Z. T. Xu, H. Z. Ke and X. J. Zhu, *ACS Appl. Energy Mater.*, 2022, **5**,
- 1417 7473-7478.
- 1418 198. Y. Xiong, Y. Qin, L. Su and F. Ye, *Chem-Eur. J.*, 2017, **23**, 11037-11045.
- 1419 199. J. Chen, G. Li, N. Lu, H. Lin, S. Zhou and F. Liu, *Mater. Today Chem.*, 2022, **24**, 100832.
- 1420 200. C. Zhu, L. Lu, Q. Fang, S. Song, B. Chen and Y. Shen, *Adv. Funct. Mater.*, **33**, 2210905.
- 1421 201. J. Bi, B. Xu, L. Sun, H. Huang, S. Fang, L. Li and L. Wu, *ChemPlusChem*, 2019, **84**, 1149-
- 1422 1154.
- 1423 202. L. Wang, L. Wang, S. F. Yuan, L. P. Song, H. Ren, Y. K. Xu, M. M. He, Y. H. Zhang, H. Wang,
- 1424 Y. C. Huang, T. Wei, J. W. Zhang, Y. Himeda and Z. J. Fan, *Appl. Catal., B*, 2023, **322**, 122097.
- 1425 203. R. Xu, X. S. Wang, H. Zhao, H. Lin, Y. B. Huang and R. Cao, *Catal. Sci. Technol.*, 2018, **8**,
- 1426 2224-2230.

- 1427 204. G. C. Huang, G. Y. Lin, Q. Niu, J. H. Bi and L. Wu, *J. Mater. Sci. Technol.*, 2022, **116**, 41-49.
- 1428 205. X. Wang, Z. Fu, L. Zheng, C. Zhao, X. Wang, S. Y. Chong, F. McBride, R. Raval, M. Bilton,  
1429 L. Liu, X. Wu, L. Chen, R. S. Sprick and A. I. Cooper, *Chem. Mater.*, 2020, **32**, 9107-9114.
- 1430 206. N. Tahir, C. Krishnaraj, K. Leus and P. Van der Voort, *Polymers*, 2019, **11**, 1326.
- 1431 207. Z. Liang, H. Y. Wang, H. Zheng, W. Zhang and R. Cao, *Chem. Soc. Rev.*, 2021, **50**, 2540-2581.
- 1432 208. Y. Z. Cheng, W. Ji, P. Y. Hao, X. H. Qi, X. Wu, X. M. Dou, X. Y. Bian, D. Jiang, F. T. Li, X.  
1433 F. Liu, D. H. Yang, X. Ding and B. H. Han, *Angew. Chem. Int. Ed.*, 2023, e202308523.
- 1434 209. K. Ma, J. Li, J. Liu, C. Li, X. B. Chen, Z. Li, L. Wang, Z. Shi and S. Feng, *Appl. Surf. Sci.*,  
1435 2023, **629**, 157453.
- 1436 210. Y. Li, C. Lai, S. Liu, Y. Fu, L. Qin, M. Xu, D. Ma, X. Zhou, F. Xu, H. Liu, L. Li, Q. Sun and  
1437 N. Wang, *J. Mater. Chem. A*, 2023, **11**, 2070-2091.
- 1438 211. Z. Sun, H. Zheng, J. Li and P. Du, *Energy Environ. Sci.*, 2015, **8**, 2668-2676.
- 1439 212. N. Z. Xu, B. W. Cai, Q. Li, Y. B. Liu, J. Tang, K. Q. Wang, B. L. Xu and Y. N. Fan, *J. Alloys*  
1440 *Compd.*, 2021, **871**, 159565.
- 1441 213. L. W. Zhang, Y. M. Zhang, X. J. Huang and Y. P. Bi, *Chem. Sci.*, 2022, **13**, 8074-8079.
- 1442 214. L. Huang, D. Wang, H. Zeng, L. Zheng, S. Lai and J. P. Zou, *Nanoscale*, 2022, **14**, 18209-  
1443 18216.
- 1444 215. Y. Yan, J. Miao, Z. Yang, F. X. Xiao, H. B. Yang, B. Liu and Y. Yang, *Chem. Soc. Rev.*, 2015,  
1445 **44**, 3295-3346.
- 1446 216. Y. L. Chen, G. C. Huang, Y. N. Gao, Q. S. Chen and J. H. Bi, *Int. J. Hydrogen Energy*, 2022,  
1447 **47**, 8739-8748.
- 1448 217. C. Liu, Y. C. Wang, Q. Yang, X. Y. Li, F. L. Yi, K. W. Liu, H. M. Cao, C. J. Wang and H. J.

- 1449 Yan, *Chem-Eur. J.*, 2021, **27**, 13059-13066.
- 1450 218. Y. Chen, G. Huang, Y. Gao, Q. Chen and J. Bi, *Int. J. Hydrogen Energy*, 2022, **47**, 8739-8748.
- 1451 219. X. Xu, W. Huang, X. Li, Y. Sui, W. Chen, Y. Li, H. Ye, C. Pan, H. Zhong and M. Wen, *J. Environ. Chem. Eng.*, 2023, **11**, 109331.
- 1452
- 1453 220. C. Lu, J. Yang, S. Wei, S. Bi, Y. Xia, M. Chen, Y. Hou, M. Qiu, C. Yuan, Y. Su, F. Zhang, H. Liang and X. Zhuang, *Adv. Funct. Mater.*, 2019, **29**, 1806884.
- 1454
- 1455 221. P. Su, K. Iwase, T. Harada, K. Kamiya and S. Nakanishi, *Chem. Sci.*, 2018, **9**, 3941-3947.
- 1456 222. J. Roeser, K. Kailasam and A. Thomas, *Chemsuschem*, 2012, **5**, 1793-1799.
- 1457 223. X. Chen, X. Zhang, X. Xiao, Z. Wang and J. Zhao, *Angew. Chem. Int. Ed.*, 2023, **62**, e202216010.
- 1458
- 1459 224. R. Sun, X. Wang, X. Wang and B. Tan, *Angew. Chem. Int. Ed.*, 2022, **61**, e202117668.
- 1460 225. L. Ge, Y. Ke and X. Li, *Chem. Commun.*, 2023, **59**, 5795-5806.
- 1461 226. C. B. Meier, R. Clowes, E. Berardo, K. E. Jelfs, M. A. Zwijnenburg, R. S. Sprick and A. I. Cooper, *Chem. Mater.*, 2019, **31**, 8830-8838.
- 1462